Dynamical and Environmental Effects on the Optical Properties of an Heteroleptic Ru(II)–Polypyridine Complex: A Multilevel Approach Combining Accurate Ground and Excited State QM-Derived Force Fields, MD and TD-DFT

Giacomo Prampolini, Francesca Ingrosso, Alekos Segalina, Stefano Caramori, Paolo Foggi, Mariachiara Pastore

To cite this version:

Giacomo Prampolini, Francesca Ingrosso, Alekos Segalina, Stefano Caramori, Paolo Foggi, et al.. Dynamical and Environmental Effects on the Optical Properties of an Heteroleptic Ru(II)–Polypyridine Complex: A Multilevel Approach Combining Accurate Ground and Excited State QM-Derived Force Fields, MD and TD-DFT. Journal of Chemical Theory and Computation, 2019, 15 (1), pp.529-545. ⟨10.1021/acs.jctc.8b01031⟩. ⟨hal-03447261⟩

HAL Id: hal-03447261
https://hal.science/hal-03447261v1

Submitted on 24 Nov 2021

Dynamical and environmental effects on the optical properties of an heteroleptic Ru(II)-polypyridine complex: a multilevel approach combining accurate ground and excited state QM-derived force fields, MD and TD-DFT

Giacomo Prampolini,[a,*] Francesca Ingrosso,[b,*] Alekos Segalina,[b] Stefano Caramori[c]
Paolo Foggi,[d,e,f] and Mariachiara Pastore[b,g,*]

[a] *Istituto di Chimica dei Composti OrganoMetallici* (ICCOM-CNR),
Area della Ricerca, via G. Moruzzi 1, I-56124 Pisa, Italy
[b] *Université de Lorraine, Laboratoire de Physique et Chimie Théoriques* (LPCT),
Boulevard des Aiguillettes, BP 70239 54506 Vandoeuvre-lès-Nancy Cedex, France
[c] *Dipartimento di Scienze Chimiche e Farmaceutiche,* Università degli Studi di Ferrara,
Via Luigi Borsari 46, I-44100, Ferrara, Italy
[d] *European Laboratory for Non Linear Spectroscopy (LENS)*, Università di Firenze,
Via Nello Carrara 1, I-50019 Sesto Fiorentino, Florence, Italy
[e] *INO-CNR, Istituto Nazionale di Ottica*, Consiglio Nazionale delle Ricerche,
Largo Fermi 6, I-50125 Florence, Italy
[f] *Dipartimento di Chimica, Biologia e Biotecnologie*, Università di Perugia,
Via Elce di Sotto 8, I-06123 Perugia, Italy
[g] *CNRS, Laboratoire de Physique et Chimie Théoriques* (LPCT),
Boulevard des Aiguillettes, BP 70239 54506 Vandoeuvre-lès-Nancy Cedex, France

November 26, 2018

---

[*] giacomo.prampolini@pi.iccom.cnr.it, francesca.ingrosso@univ-lorraine.fr, mariachiara.pastore@univ-lorraine.fr

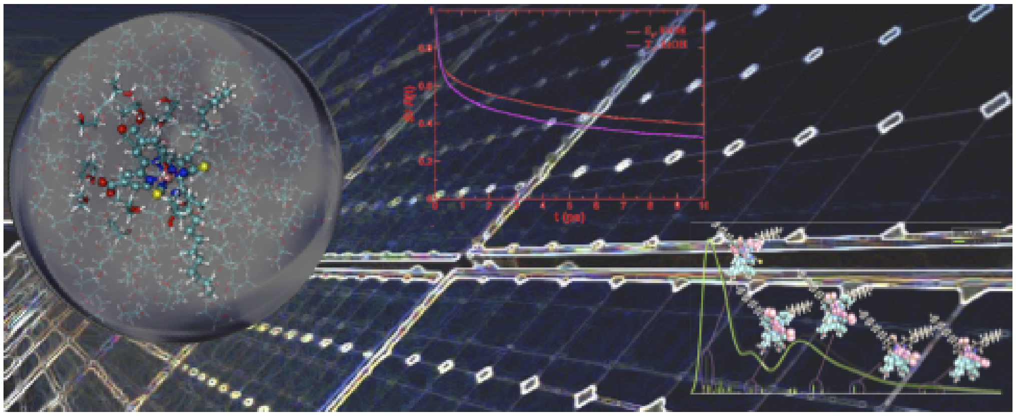

Abstract

An integrated multilevel approach is here built by combining classical Molecular Dynamic (MD) simulations, Time-Dependent Density Functional Theory (TD-DFT) calculations and solvation dynamics linear response (LR) analysis, and successively employed to investigate the optical properties and solvation structure of a prototypical heteroleptic Ru(II)-polypyridyl complex, widely employed in dye sensitized solar cells. The MD simulations are performed with an accurately parameterized intramolecular force field (FF), specifically derived from the quantum chemical (DFT) description of the molecule, both for its singlet and triplet ground states. Solvent effects, in ethanol (EtOH) and dimethyl sulfoxide (DMSO), are taken into account at different level of approximation, going from a totally implicit description (polarizable continuum) to an hybrid explicit/implicit scheme. Our results show that the developed FFs were able to accurately describe and preserve the octahedral coordination of the Ru(II) center along the MD trajectories, yielding an accurate picture of the solute dynamics. Noticeably, the dynamical effects and the inclusion of an explicit micro-solvation shell were found to be crucial to get a good agreement with the experimental absorption spectrum in EtOH, in both shape and positions of the main bands. The significant experimental blue-shift of the two low-energy bands in DMSO, that is not reproduced by the simulated thermal-averaged spectra, is, instead, attributed to de-protonation phenomena of the carboxylic groups induced by the strong nucleophilic character of the solvent. Finally, analysis of the solvent response shows that the structural changes in the first solvation shell, following the metal-ligand to ligand charge transfer excitation, cause, in the protic medium (EtOH) the breakdown of the linear response approximation, which, on the contrary, holds for DMSO.

1 Introduction

Charge transfer processes induced by light absorption are crucial in a variety of physico-chemical phenomena in different fields, ranging from the natural and artificial photosynthesis,[1,2] photovoltaic applications[3,4] and photo-activated medical therapies.[5,6] Since the first report in 1960s by Crosby and co-workers[7] on the luminescence of $Ru(bpy)_3{}^{2+}$ and the following breakthrough paper in 1972 by Gafney and Adamson,[8] in which the electron transfer (ET) quenching of the triplet charge transfer (CT) excited state was demonstrated, octahedral ruthenium polypyridine complexes have been extensively studied and exploited by virtue of their peculiar chemical and photochemical properties.[9–12] In particular, they have been largely employed in dye sensitized solar cells (DSCs), where the outstanding performances of the [Ru(4,4′-COOH-2,2′-bpy)$_2$(NCS)$_2$] (N3) dye and its derivatives, have played a central role in the success of the DSCs technology.[13–18] When dealing with CT excitations, it is clear that the surrounding solvent molecules, responding to the sudden change in the solute's charge distribution, play an important role on both the energetics and dynamics of the excited states.[19–27]

From a theoretical and computational point of view, a proper treatment of the environment as well as of its dynamical response to the change of the electron density distribution upon electronic excitation is therefore crucial for a reliable description of any photochemical and photophysical process. This evidently requires to go beyond an implicit description of the surrounding medium,[28] by explicitly including the solvent molecules into the system.[29,30] Although the increasing computational power and the implementation of efficient parallel algorithms make full *ab initio* molecular dynamic (MD) simulations of rather complex systems affordable,[26,27,31,32] the necessity of treating a large number of solvent molecules on longer timescales often limits the feasibility of first-principles MD methodologies. To circumvent the first limitation, *i.e.* the system size, a possible solution is to resort to hybrid Molecular Mechanics (MM) and Quantum Mechanics (QM) schemes (QM/MM), where the solute is described at QM level and the solvent molecules by means of classical mechanics.[33–36] Although these approaches allow for quite accurate *ab initio* MD simulations of large molecules in solution, at present only runs of the order of picoseconds can be reasonably carried out. Yet, as far as the second of the aformentioned computational limits (the simulation time length) is concerned, to achieve a meaningful statistical analysis of the solvent structure as well as of its dynamic response to the solute electronic excitation, one has to necessarily resort to classical techniques as Molecular Dynamics (MD) or MonteCarlo (MC) where much longer runs (> 1 ns) can be carried out .

In classical MD or MC simulations,[37–39] the description of the investigated system is encoded in the parameters of a collection of analytical model functions, the force-field (FF), which gives an estimate of the system's total energy depending on the nuclei positions. In other words, the reliability of the classical simulations essentially relies on the FF accuracy.[40–47] For this reason, the selection of an appropriate FF to investigate the solvation structure around the considered Ruthenium complex and its dynamics upon electronic excitation should be taken and validated with care. In fact, the straighfoward adoption of literature transferrable parameters was readily discarded, given both the scarce availability of FFs able to describe metal-organic compounds and the lack of FFs capable to handle the molecule in an excited electronic state.[48] An alterantive route consists in tailoring a specific FF for the investigated molecule, by deriving the FF parameters from a QM description of the target system. Such Quantum Mechanically Derived FFs (QMD-FFs) have indeed attracted a lot of attention in the past decade,[44,49–67] and several different approaches and parameterization techniques have been reported. In the present paper, we resort to the JOYCE protocol,[51] developed and recently refined[54,67] by some of us. As a matter of fact, the QMD-FFs produced by JOYCE were already succefully employed to study the solvation features of two organo-metallic complexes in octahedral symmetry, namely the ferro- and ferri-cyanide ions.[68] On the same foot, one of the major strengt of the JOYCE code stands in its capability of parameterizing FFs for any electronic excited state, exploiting the possibility of describing excited potential energy surface through the time dependent (TD) implementation of suitable DFT methods. Indeed, up to present, excited state QMD-FF, parameterized by means of the JOYCE code, were successfully employed in the simulation of singlet excited states of several organic dyes, in simple solvents[46,69–73] or embedded in more complex environments.[74–76] These previous results prompted us to build, by means of the JOYCE code, two specific QMD-FFs for the investigated Ru-complex, one for the ground-state and one for its lowest triplet excited state. It might be worth noticing that, up to our knowledge, this is the first FF specifically built for a triplet state.

Exploiting the developed FFs, here we set up an integrated multilevel computational strategy, which combines classical MD simulations with extensive excited state TD-DFT calculations, to simulate the steady-state absorption properties and analyze the solvation dynamics of the well-known Z907 dye, $[(NCS)_2Ru(bpy\text{-}(COOH)_2)(bpy\text{-}(C_6H_{13})_2)]$ (Figure 1), embedded in both a protic (EtOH) and an aprotic (DMSO) solvent. Indeed, in a recent paper reported by some of us,[30] peculiar transient IR and visible spectral evolutions were observed only in the former solvent, and interpreted as arising from the change in the Z907-ethanol hydrogen-bond network, following the transition to the lowest-energy triplet state, which displaces charge from the NCS ligands to the bpy-COOH moiety. In the present work , to get deeper insights into the response of the two solvents to the CT electronic excitation, we first analyze the outcomes of the MD simulations in terms of the solvent microscopic structure and its relaxation dynamics in both the ground, S_0, and excited lowest triplet state, T_1, in a linear response (LR) framework. Next, we obtain thermally averaged absorption spectra, by computing the vertical excitation energies at TD-DFT level over a large number of snapshots extracted from the MD trajectories. During each calculation, the solvent was accounted for either at implicit level or by explicitely including at QM level a number of solvent molecules, selected on the grounds of the

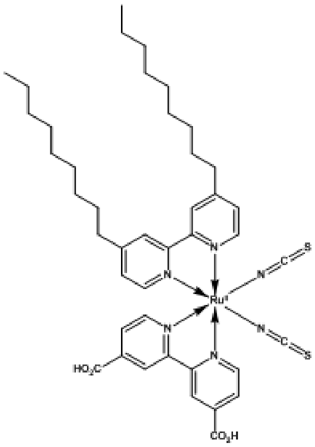

Figure 1: Chemical structure of the Z907 dye.

solvation structure analysis. It is worth to stress that, to the best of our knowledge, this is the first time that the dynamical and solvation effects are deeply analized and simultaneosly taken into account, in a statistically meaningful manner, in the simulation of the optical absorption spectra of a Ru(II)-polypyridyl complex. It is worth to stress that a previous work by Assfeld and co-workers[77] reported a combined classical MD and mixed QM/MM approach to simulate the absorption spectrum in water of a Ru(II) sensitizer. Due to the lack of accurate FFs for the octahedral transition metal compounds, however, the MD trajectory was carried out by freezing the solute geometry and, then, QM/MM optimizations of the solute were performed on the randomly extracted configurations to partially recover the structural response of the solute to the solvent distribution.

The paper is organized as follows: in the next section the adopted multi-level approach is discussed, together with the relevant computational details for each of the employed QM and MM techniques; the results are then reported and discussed in the third section, whereas our main conlusion are drawn in the last section.

2 Methodology

The multilevel approach adopted in this work is schematically depicted in Figure 2: for S_0 and T_1, the intramolecular FF is parameterized through the JOYCE code,[51,54] on the basis of QM (DFT) calculations as detailed below; the intermolecular part (solute-solvent and solvent-solvent) is taken from the Optimized Potentials for Liquid Simulations (OPLS) FF, with the solute point charges calculated at DFT level on the geometries optimized in a polarizable continuum dielectric medium;[78] the S_0 MD trajectories in explicit solvent are sampled by extracting representative solute@solvent conformations, which were in turn successively employed for the calculations of the steady-state thermal-averaged absorption spectra; the EtOH and DMSO dynamics along the S_0 and T_1 MD runs is analyzed in a linear response framework.

2.1 QMD-FF parameterization

The intramolecular QMD-FF employed for the description of Z907 flexibility, E^{intra}, takes the standard form:

$$E^{intra} = E^{stretch} + E^{bend} + E^{Rtors} + E^{Ftors} + E^{nb} \tag{1}$$

The first two terms account for the stretching and bending contributions, and are both computed as sums of harmonic functions:

$$E^{stretch} = \frac{1}{2}\sum_{\mu}^{N_s} k_{\mu}^{s}(r_{\mu} - r_{\mu}^{0})^2;\; E^{bend} = \frac{1}{2}\sum_{\mu}^{N_b} k_{\mu}^{b}(\theta_{\mu} - \theta_{\mu}^{0})^2 \tag{2}$$

being k_{μ}^{s}, k_{μ}^{b} and $r_{\mu}^{0}, \theta_{\mu}^{0}$ the force constants and the equilibrium values. On the same foot, selected stiff torsional internal coordinates,[51,54] as those displayed in panels b)-d) in Figure 3, were also accounted for through a sum of harmonic functions as

$$E^{Rtors} = \frac{1}{2}\sum_{\mu}^{N_{Rt}} k_{\mu}^{t}(\phi_{\mu} - \phi_{\mu}^{0})^2 \tag{3}$$

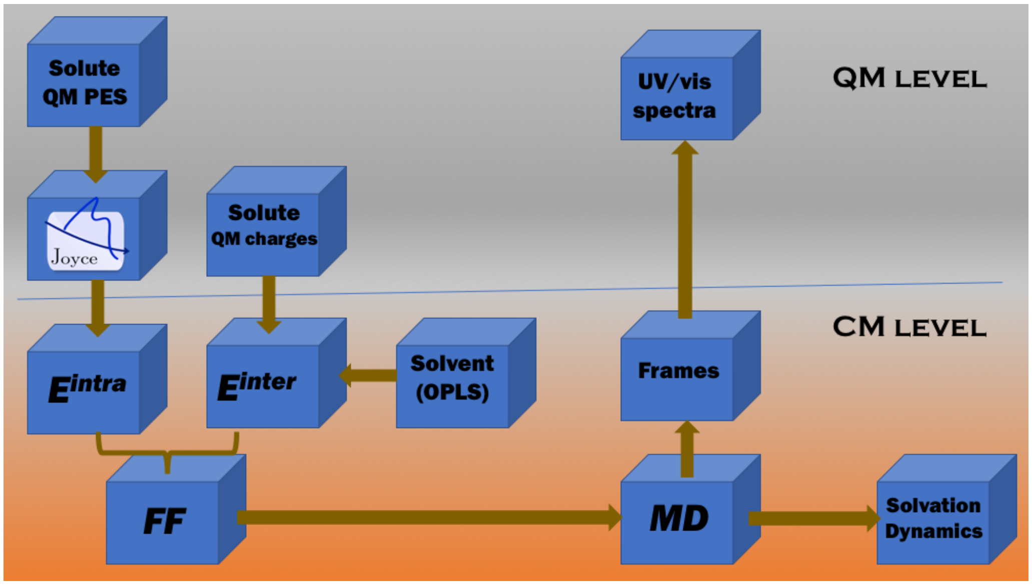

Figure 2: Scheme of the integrated sequential approach. Quantum Mechanics (QM) and Classical Mechanics (CM) levels are evidenced by gray and orange backgrounds, respectively. Brown arrows indicate the sequential data flux. The same protocol has been applied to ground (S_0) and excited (T_1) states.

being k^t_μ and ϕ^0_μ the force constant and the equilibrium values of the considered stiff dihedral. To account for the more flexible δ_1-δ_7 dihedrals (see panels e) and f) in Figure 3 for definition), a sum of cosines is used, namely

$$E^{Ftors} = \sum_{\mu}^{N_{Fdihedrals}} \sum_{j=1}^{N_\mu} k^d_{j\mu} \left[1 + cos(n^j_\mu \delta_\mu - \gamma^j_\mu)\right] \tag{4}$$

where $k^d_{j\mu}$ is the force constant, δ_μ the dihedral, n^j_μ and γ^j_μ the multiplicity and a phase factor for the j^{th} cosine. N_μ is the number of cosine functions employed for dihedral μ. The last term of equation (1) is computed as

$$E^{nb} = \sum_{i=1}^{N_{sites}} \sum_{j=1}^{N_{sites}} \left[E^{LJ\ intra}_{ij}\right] \tag{5}$$

where the interaction between the ith and jth atoms is described through a 12-6 Lennard Jones (LJ) potential ($E^{LJ\ intra}$).

Both S_0 and T_1 intramolecular QMD-FFs were parameterized with the JOYCE package,[51,54] through a least square minimization of the objective function I^{intra}

$$I^{intra} = \sum_{g=0}^{N_{geom}} W_g \left[U_g - E^{intra}_g\right]^2 + \sum_{K \le L}^{3N-6} \frac{2W''_{KL}}{(3N-6)(3N-5)} \left[H_{KL} - \left(\frac{\partial^2 E^{intra}}{\partial Q_K \partial Q_L}\right)\right]^2_{g=0} \tag{6}$$

where N_{geom} is the number of the sampled conformations, Q_K is the K^{th} normal coordinate and U_g is the QM computed energy in the g^{th} geometry, with respect to the absolute minimum ($g = 0$). The QM Hessian matrix H_{KL} and the FF Hessian are evaluated at $g = 0$. W_g and W''_{KL} are the standard[51,54] weighting factors for energies and Hessian, respectively. Further details can be found in the Supplementary Information and in the original papers.[51,54] The GAUSSIAN09 suite of programs[79] has been used to perform all the required QM calculations.

Geometry optimizations of the Z907 dye were carried out in the gas phase with the B3LYP[80] functional and the DGDZVP[81] basis set, at restricted and unrestricted level for S_0 and T_1, respectively. In fact, besides the average good performances reported for the B3LYP functional in handling in general transition metal complexes,[82–85] the here adopted B3LYP/DGDZVP level of theory has been proved valuable in investigating Ru polypyridine compounds.[18,86] Finally, as discussed in the next sections, this choice is consistent with the level of theory employed to study its electronic transitions. For these optimized conformations, Hessian matrices and harmonic vibrational frequencies were calculated at the same level of theory. Furthermore, relaxed energy scans along the δ_1-δ_7 flexible dihedrals (see Figure 3) were performed for both investigated states by varying each dihedral angle from 0° to 180°, in steps of 15°.

To model both the solute-solvent and solvent-solvent interactions, the standard 12-6 LJ (E_{ij}^{LJ}) plus charge-charge Coulomb potential (E_{ij}^{Coul}) were adopted:

$$E_{ij}^{LJ}(r_{ij}) = 4\varepsilon_{ij}\left[\left(\frac{\sigma_{ij}}{r_{ij}}\right)^{12} - \left(\frac{\sigma_{ij}}{r_{ij}}\right)^{6}\right] \tag{7}$$

and

$$E_{ij}^{Coul}(r_{ij}) = \frac{q_i q_j}{r_{ij}} \tag{8}$$

In particular, the solute-solvent intermolecular energy, $E^{FF_{inter}}$, is expressed as

$$E^{inter}(\bar{r}) = \sum_{i=1}^{N_{Z907}} \sum_{j=1}^{N_{solv}} \left[E_{ij}^{LJ}(r_{ij}) + E_{ij}^{Coul}(r_{ij})\right] \tag{9}$$

where N_{Z907} and N_{solv} are the number of the solute and solvent interaction sites and i/j is the i^{th}/j^{th} site of the solute or solvent, respectively. LJ intermolecular parameters for both solute and solvent were taken from the OPLS FF.[39,87,88] The solute CM5 atomic point charges[89] were obtained from the equilibrium S_0 and T_1 geometries obtained at B3LYP/DGDZVP level of theory, describing the solvent (EtOH or DMSO) through the conductor-like polarizable continuum model (C-PCM).[90] Conversely, the OPLS description[39,87,88] was adopted for both solvent charges and internal flexibility. All intermolecular parameters and a complete list of the point charges obtained for the Z907 molecule in either the $S0$ and T_1 state can be found in Table J in the Supporting Information.

2.2 MD calculations

All MM and MD calculations were performed with the GROMACS engine.[91,92] Several validation tests of the parameterized FF were performed at MM level on the isolated molecule, consisting in both MD runs in the NVT ensemble and geometry optimizations. The latter were carried out by optimizing all degrees of freedom or by performing a relaxed MM scan along a chosen dihedral. In all cases, the conjugate gradient algorithm available within the GROMACS 5.1 package[91,92] was exploited.

The simulation boxes in our MD runs of the solvated systems were composed of one Z907 molecule, in either its S_0 or T_1 state, and 1177 and 971 solvent molecules, for EtOH and DMSO, respectively. During equilibration, each system was simulated for 2.5 ns, in the NPT ensemble at 1 atm and 298 K, keeping the temperature and pressure constant through the Berendsen thermostat and barostat,[93] with τ_T and τ_P to 0.1 and 5.0 ps, respectively. At this stage, bond lengths are constrained at their equilibrium value using the LINCS algorithm, allowing for a 1 fs time step. The 5 ns production runs for each of the four resulting equilibrated systems (hereafter labeled S_0@EtOH, T_1@EtOH, S_0@DMSO and T_1@DMSO) were carried out again in the NPT ensemble, but through velocity-rescale thermostat[94] and the Parrinello-Rahman scheme.[95] During the production runs, the constraints on the stretching motions were removed and the time-step consequently decreased to 0.25 fs. In all equilibration and production simulations, a cut-off of 11 Å was employed for both charge-charge and LJ terms, whereas long-range electrostatics was accounted for through the particle mesh Ewald (PME) procedure. Along the S_0@EtOH and S_0@DMSO production runs, the trajectory was stored every 5 ps, and thereafter exploited for the extraction of 100 frames (one every 50 ps), then used for the calculation of the visible absorption spectrum (*vide infra*).

As detailed in the following, for the calculations of the solvent response function (*SRF*), four additional runs (each consisting in 5 ns) were also carried out in the micro-canonical NVE ensemble, employing the same simulation conditions adopted in the NPT production runs, but storing the trajectories every 20 fs.

2.3 Solvation Analysis

The microscopic structure of the solvated Z907 molecule was first analyzed, over the 5 ns NPT trajectories, in terms of: i) atomic pair correlation functions, $g_{\alpha\beta}(r)$; ii) average number of Hydrogen Bonds (HBs) established between the solvent molecules and the specific groups of the solute able to give HB (COOH and NCS). Each HB is identified based on geometrical parameters, namely the Donor-Acceptor distance (R_{DA}, cutoff 3.5Å), and the Acceptor-Donor-Hydrogen angle (α_{DHA}, cutoff 30°).

Thereafter, the solvation dynamics of both solvents upon excitation was analyzed through the calculation of the solvation response function (*SRF*), using a well established relationship that is based on linear response theory.[96,97] The applied expression allows for computing a non-equilibrium decay from the time correlation function of the fluctuations of the corresponding equilibrium property and originally comes from a generalization of the fluctuation-dissipation theorem.[98] In our case, we monitored the fluctuations of the difference in the solute-solvent electrostatic interaction energy, calculated at each time step of the MD NVE simulations from the Coulomb term as:

$$\Delta E = \frac{1}{4\pi\varepsilon_0}\sum_{i>j}\frac{\Delta q_i q_j}{r_{ij}}, \tag{10}$$

where Δq_i represents the difference between the excited and the ground state atomic charge on site i of the solute and q_j represents the atomic charge on the j atom of the solvent, r_{ij} is the instantaneous distance between atoms i and j, ε_0 being the vacuum dielectric permittivity.

The solvation response function was thus obtained as:

$$SRF_{S_0,T_1}(t) = \frac{< \delta\Delta E(0)\delta\Delta E(t) >_{S_0,T_1}}{< |\delta\Delta E|^2 >_{S_0,T_1}}, \tag{11}$$

where the $< ... >$ symbols at the numerator denote the time correlation function of the fluctuations of ΔE, the expression in the denominator represents the normalization factor ($|\delta\Delta E|^2$ being the ensemble average of the fluctuations), and the subscripts $_{S_0,T_1}$ mean that the calculation is performed along the equilibrium trajectory of the solute in the S_0 or T_1 state, respectively. The ground and excited state decays are expected to give very similar features if the linear response approximation hypothesis is fulfilled, and to occur on different timescales if such an approximation does not hold. The solvent relaxation dynamics were analyzed by fitting the calculated solvation response functions to a normalized linear combination of three exponentials according to:

$$SRF(t) \simeq a_1 e^{-\frac{t}{\tau_1}} + a_2 e^{-\frac{t}{\tau_2}} + a_3 e^{-\frac{t}{\tau_3}}, \tag{12}$$

with the constraint $a_1 + a_2 + a_3 = 1$. This function was chosen as the one giving the best fit based on the statistical analysis. Then, using the fitted expression, the average time constant, or correlation time, can be calculated as:

$$< \tau >= \int_0^\infty SRF(t)dt \simeq \sum_{i=1}^{3} a_i \tau_i. \tag{13}$$

2.4 Calculation of the UV-Vis spectra

All the TD-DFT calculations have been performed with the Gaussian09 package,[79] employing the B3LYP[80] exchange and correlation functional and the DGDZVP basis set, while bulk solvation effects have been described within the C-PCM approximation.[90] This protocol has been already widely validated to accurately reproduce the optical and redox properties of a variety of Ru(II)-polypyridine compounds.[17,99,100]

A preliminary assessment of the accuracy of the calculated excited states on the optimized FF ground state structure has been made by comparing the calculated absorption spectrum with that obtained by using the reference Z907 QM ground state geometry. Dynamical and explicit solvation effects, then, were simulated by calculating the electronic absorption spectra of of Z907 in S_0@EtOH and S_0@DMSO, by averaging over the 100 snapshots extracted from the MD runs. The thermal-averaged absorption spectra were then obtained by Gaussian convolution ($\sigma = 0.1eV$) of the vertical excitation energies calculated on the various snapshots extracted from the MD simulations, considering the 70 lowest transitions for each frame. Each extracted configuration contained the solute coordinates and the geometries of all solvent molecules found within a chosen distance from the solute regions more involved in HBs and strong interactions with the embedding, namely the metal atom and the NCS and COOH groups. Such threshold is chosen on the grounds of the first peak positions of the aforementioned $g_{\alpha\beta}(r)$ functions, computed between the relevant atoms, over the MD trajectories. Based on this findings, all solvent molecules within 4.0 Å from the Z907's metal (Ru), plus those molecules being 3.5 Å far from either the NCS or the COOH group, were explicitely included in the TD-DFT calculations. Finally, the so-defined QM layer (solute+solvent) was surrounded by a continuum solvent (either EtOH or DMSO), as described in the C-PCM method.[90] Analysis of the excited states character giving rise to the main spectral features in the "static pictures" and along the MD trajectories has been carried out with the TheoDORE package.[101,102]

3 Results

3.1 FF assessment

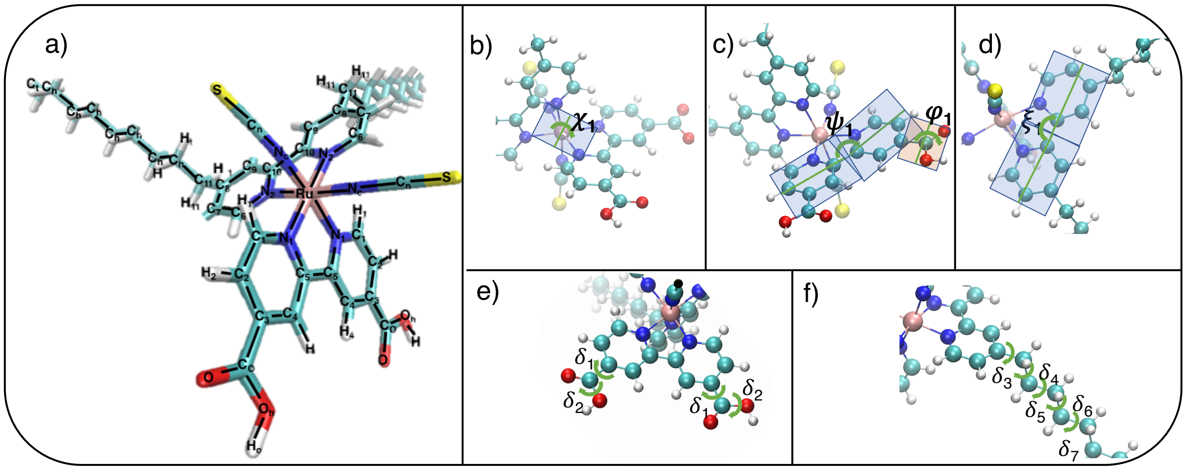

Figure 3: Panel a): Z907 structure and FF atom labels; Panels b)-d): stiff dihedral defining the octahedral structure around the metal (panle b),χ_n with $n = 1-3$, for each $N-N-N-N$ quadruplet), the coplanarity of the aromatic rings of the pyridine bearing the $-COOH$ group (panle c), ψ_n, $n = 1,2$), the coplanarity of the $-COOH$ group with the attached phenyl ring (panle c), ϕ_n with $n = 1-2$, for each ring), the coplanarity of the aromatic rings of the pyridine bearing the alkyl chains (panel d) ξ_n, $n = 1,2$). Panels e) and f): flexible dihedrals involving the $-COOH$ group (panle e), δ_1 and δ_2) and the aryl-alkyl linkage (panel f), δ_3)

As detailed above, the intramolecular QMD-FFs for the S_0 and T_1 electronic states of the Z907 complex were separately parameterized by means of the JOYCE code, based on the QM data. In both cases, the same atom types (shown in panel a), Figure 3) and the same collection of internal coordinates (as for instance those displayed in panels b)-f), Figure 3) were adopted; further details on the parametrization procedure are given in the Supporting Information. Here it might be worth noticing that the S_0 and T_1 FFs have identical expressions, but differ in both the intramolecular parameters entering equations (2)-(5) and in the intermolecular point charges of equation (8) The latter were directly transferred from the atomic charges obtained from the electronic densities computed at DFT level for the ground and triplet state, respecitvely. Both parameterization ended successfully, obtaining a standard deviation of 0.17 kJ/mol for S_0 and 0.16 kJ/mol for T_1. The list of all the parameters for both states is reported in detail in Tables A-I, in the Supporting Information.

A first important assessment on the quality of the FF parametrization, can be obtained by

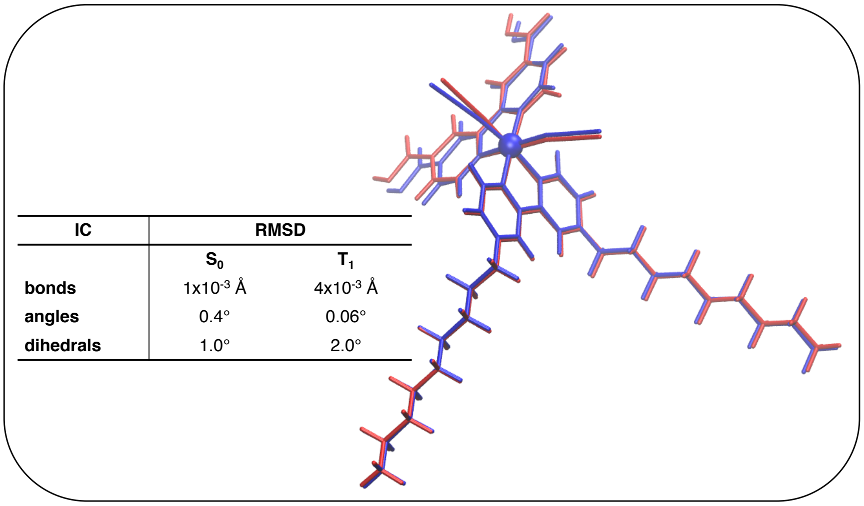

IC	RMSD	
	S_0	T_1
bonds	1x10^{-3} Å	4x10^{-3} Å
angles	0.4°	0.06°
dihedrals	1.0°	2.0°

Figure 4: Left: RMSD computed between the DFT optimized S_0 and T_1 structures and the one obtained with an MM optimization performed with the two JOYCE FFs. The last row refers to the RMSD computed with respect the normal modes of each optimized conformation; Right: S_0 MM and FF optimized structures.

comparing the Root Mean Square Displacement (RMSD) between the QM and QMD-FF S_0 and T_1 optimized structures, displayed in Figure 4. As is apparent, an excellent agreement is found for all IC, in terms of bonds, angles and dihedrals. The large dimensions and noticeable chain flexibility of the Z907 molecule, however, justify the fact that a rather small error in the dihedral RMSD ($\sim$1-2°), translates into slightly higher ($>$0.1 Å), RMSD values evaluated in terms of normal modes.

Proceeding further with the comparison between the QMD-FF and QM description, in the top panel of Figure 5, the Z907 vibrational frequencies, computed either at QM level (cyan circles) or through the S_0 QMD-FF (blue squares), are compared. A remarkable agreement appears for most frequencies, with the best results observed for the highest frequencies, whose QM modes are essentially localized over the corresponding FF ICs, as evidenced by their overlaps reported in the top part of the panel. Similar results were obtained for the T_1 state, displayed in detail in Figure B in the Supporting Information.

In the bottom panel of Figure 5, the QM relaxed scans of selected flexible dihedrals (see Figure 3 for definitions) are compared to their MM counterparts. Notice that for the Z907 molecule symmetry was exploited during parameterization, thus forcing the same set of parameters to describe the same dihedral angle in identical parts of the molecules (*e.g.* the two COOH torsions), so for the sake of clarity, only one dihedral for each pair is reported in Figure 5. Furthermore, as confirmed by the quasi identical shapes of the δ_6 and δ_7 QM profiles, to save computational time, the rest of the aliphatic chain dihedrals (δ_8-δ_{10}) was not parameterized over a QM energy curve, but constrained to coincide with the δ_7 MM profile by imposing the same parameters

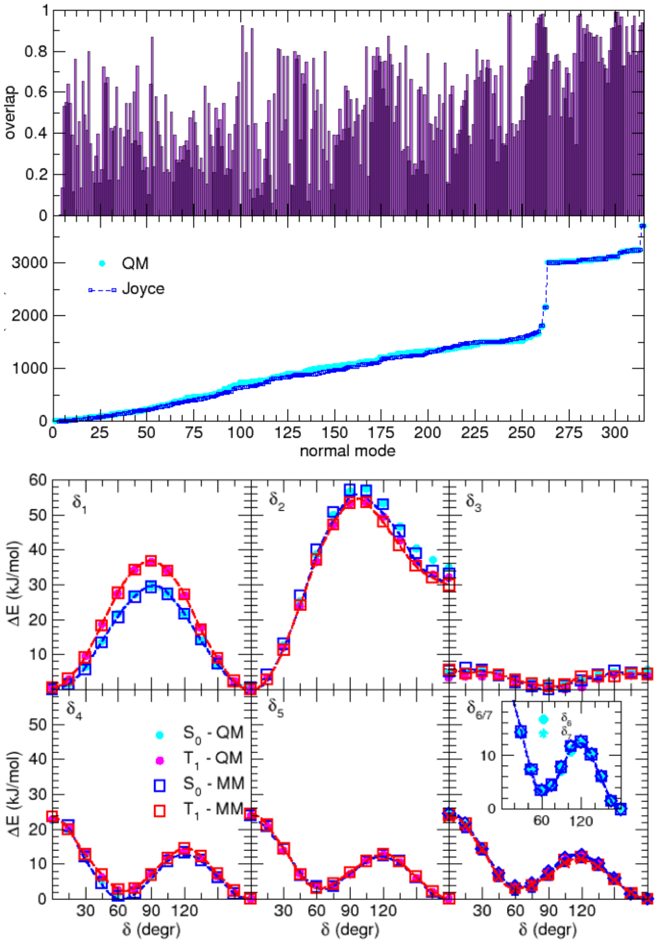

Figure 5: Top panel: Overlap between the S_0 QM and FF normal modes (top); S_0 QM vibrational frequencies (cyan solid circles) *vs.* their FF counterparts (blue squares) (bottom); Bottom panel: Comparison between QM torsional relaxed energy scans (cyan and magenta full circles, for S_0 and T_1, respectively) and MM relaxed profiles (blue and red empty squares), obtained for all Z907's flexible dihedral.

during the QMD-FF fitting. By looking at the results displayed in Figure 5, the overall high quality of the QMD-FF in representing flexible torsions emerges. It is worth to recall, here, that the nature of the low-lying electronic transitions in these heteroleptic systems is of ligand-metal (NCS-Ru) to ligand (bypyridine functionalized with the COOH groups anchored to the TiO_2 surface in DSSCs) charge transfer character (LML$'$CT), thus allowing for an efficient electron flow toward the semiconductor and for the concomitant positive charge being localized far from the interface.[18,30,99,100] Thus, the dihedrals on the aliphatic chains distant from the region interested by the excitation (δ_3-δ_6) do not show significant difference between their S_0 and T_1 profiles. On the other hand, not surprisingly, appreciable small differences appear in the δ_1 and, to a lesser extent, δ_2 QM profiles, being very well reproduced by both the S_0 and T_1 QMD-FFs. The increased steepness of the δ_1 energy curve clearly originates from the increased π character of the C-COOH bonds accepting the charge moving from the Ru-NCS ligands. A quantitative estimation of this CT can be found in Table K in Supporting Information, where the CM5 charges of selected moieties (*i.e.* the metal atom (Ru), the thio-cyano groups (NCS), the rings of the bipyridines bearing the alkyl chain (Φ-alkyl) or the carboxyl group (Φ-COOH) and the latter group itself (COOH)) computed at QM level on the S_0 and T_1 optimized geometries in different solvents are reported. Whithin an implicit treatment of the environment, as expected, no appreciable differences in the amount of transferred charge are found, with a sizeable global charge depletion involving the Ruthenium atom and the NCS groups (about 0.2 e^-), which is essentially transferred on the bipyridine bearing the carboxyl group and only partially (ca. 0.08 e^-) to the COOH anchoring moieties.

3.2 Dynamical properties and solvation analysis

Having assessed the reliability of the parameterized FFs, the analysis of the MD trajectories performed in standard conditions on the S_0@EtOH, T_1@EtOH, S_0@DMSO and T_1@DMSO systems provides us with information about the structural changes of the solute dissolved in the two solvents, both in its electronic ground state and lowest triplet excited state. A first visual inspection of the MD runs discloses that in all cases the Z907 backbone structure was preserved, although large amplitude motions of the alkyl chains characterized the system dynamics.

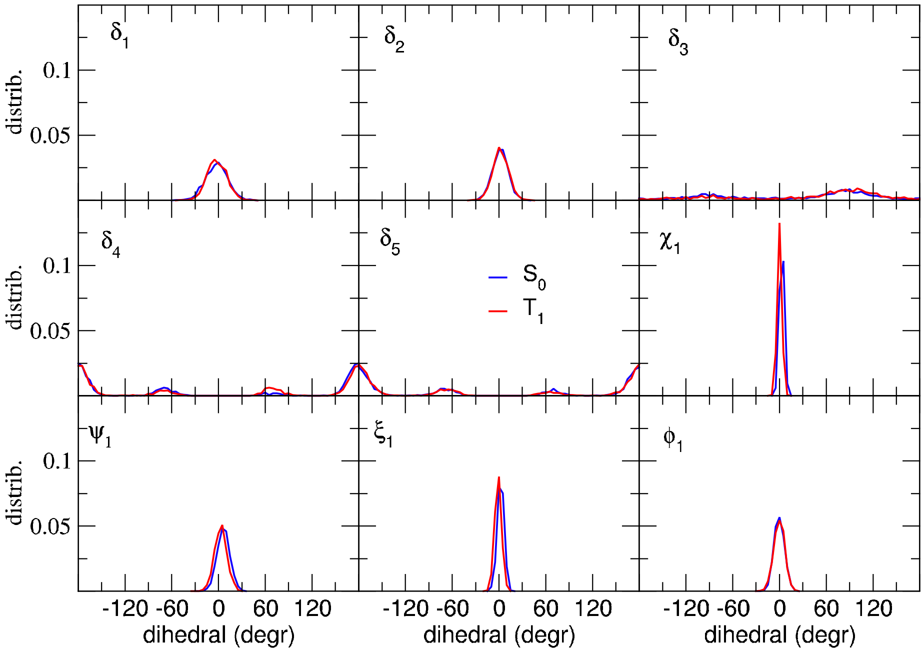

Figure 6: Dihedral distributions computed over the S_0@EtOH and T_1@EtOH (red) MD runs. The labels of the δ flexible dihedrals as well as of the χ, ψ, ξ and ϕ dihedrals, governing the planarity of different Z907 moieties, are given in Figure 3.

Figure 6 displays the population of several selected dihedrals during both the S_0@EtOH (blue) and T_1@EtOH dynamics. Quantitatively similar results were achieved in DMSO, as shown in Figure D in Supporting Information. The first general observation is that the effect of the electronic transition is negligible for all investigated dihedrals. The flexible dihedrals belonging to to the alkyl chain (δ_3 to δ_{10}) explore large portions of the accessible phase space, thus populating significantly all *trans* and *gauche* conformers, both in the ground and in the excited state. Concerning the dihedrals at the COOH groups (δ_1 and δ_2), they span a rather wide, $\pm 30^\circ$ range. On the other hand, the backbone structure, described by the stiff dihedrals χ, ψ, ξ and ϕ defined in Figure 3, shows contained oscillations around the values corresponding to those of the equilibrium QM geometry, and this behavior is practically identical in the excited state.

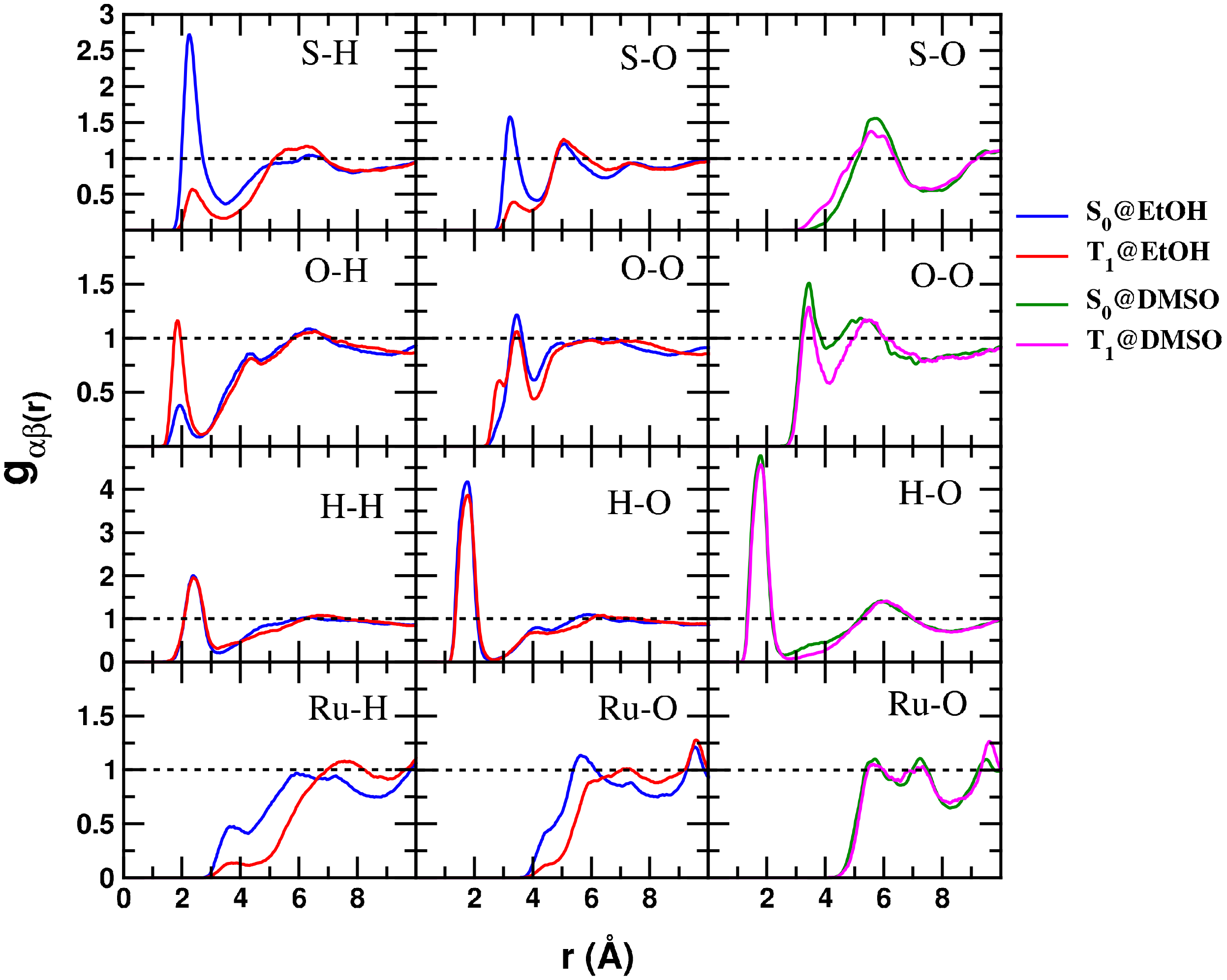

Figure 7: Atomic pair correlation functions $g_{\alpha\beta}(r)$ between Z907 atoms (α) and the solvent proton donor/acceptor atoms (β) (H atom of EtOH - left panels, O atom of EtOH - central panel, O atom of DMSO - right panel). The interactions of the S atom of the thiocyanate group, of the O and H atoms of the carboxyl groups, and of the Ru atom are reported in the top, middle and bottom panels, respectively. Ground and excited state results are reported in different colors according to the legend.

The octahedral symmetry of the metal-ligand network and the coplanarity of the bipyridine rings is thus conserved in the transition.

To get a detailed picture about the organization of the solvent around the ground and triplet excited state solute, in Figure 7 we report the most significant pair correlation functions computed for our systems. The most relevant result is indeed the difference in the molecular organization of the two solvents around the ground state solute with respect to the excited state one. We recall here that the Ru atom and the NCS group undergo a charge depletion and that the bipyridine and the COOH groups collect the charge excess. In general, the local restructuring of ethanol after the change in the solute electron density is much more affected than in the case of DMSO. First of all, as it can be observed from the top left panel of Figure 7, the hydroxyl hydrogen atom of EtOH is involved in a strong HB with the S atom of the thiocyanate groups. This interaction is strongly weakened in the excited state and is not observed in DMSO, being an aprotic solvent.[30] In EtOH, a similar (opposite in trend) effect is observed for the HBs with the carboxyl groups (O-H panel in Figure 7), for which the solvent behaves as an acceptor. In Table 1 we report the average number of HBs around these groups. EtOH is involved in 2.2 HBs with the NCS groups in the ground state and only in 0.4 HBs in the excited state. Conversely, a much smaller change affects the HB number at the COOH group (from 2.2 to 2.7). From the pair distribution functions describing the position of the O atom of DMSO around the S atom of the NCS groups and the O atom of the carboxylic groups (upper right panels of Figure 7), we can conclude that the solvent molecules around the NCS groups are located at larger distances compared to ethanol and that the negative charge flowing toward the COOH groups in the excited state makes them more repulsive in the interaction with the O atom of the DMSO molecule, though the number of HBs established with this group remains unchanged (1.9) going from the ground to the excited state. Finally, it is worth noting that the excitation does not induce noticeable changes in the organization of DMSO around the Ru center (bottom panels in Figure 7), whereas the ethanol molecules tend to move to further solvation shells.

State	Z907		NCS		COOH	
	EtOH	DMSO	EtOH	DMSO	EtOH	DMSO
S_0	4.5	1.9	2.2	0.0	2.2	1.9
T_1	3.1	1.9	0.4	0.0	2.7	1.9

Table 1: Average number of HBs established between the Z907 solute in its ground and triplet states and the two investigated solvents. In the last two columns refer to the HBs specifically established between the solvent and the NCS and COOH functional groups.

The analysis of the changes in the local structure around the solute between the ground and the excited state allowed us to interpret the differences in the solvent dynamic of ethanol and DMSO. To begin with, we display in the top left panel of Figure 8 the results obtained for the solvation response in EtOH, calculated according to eq. (11). The first remark relates to the evident breakdown of the linear response hypothesis: since very early stages of the time dependent decay (about 0.1 ps), the function calculated from equilibrium simulations in the ground state relaxes at a different rate compared to the one calculated in the excited state. This behavior is known for solvents that give rise to relatively strong local interactions with the solute (*e.g.*, hydrogen bonds) and has been reported for different molecular systems by several groups.[103–107] In particular, different relaxation rates are associated with a different local environment interacting with the solute. For instance, a slowing down of the solvation

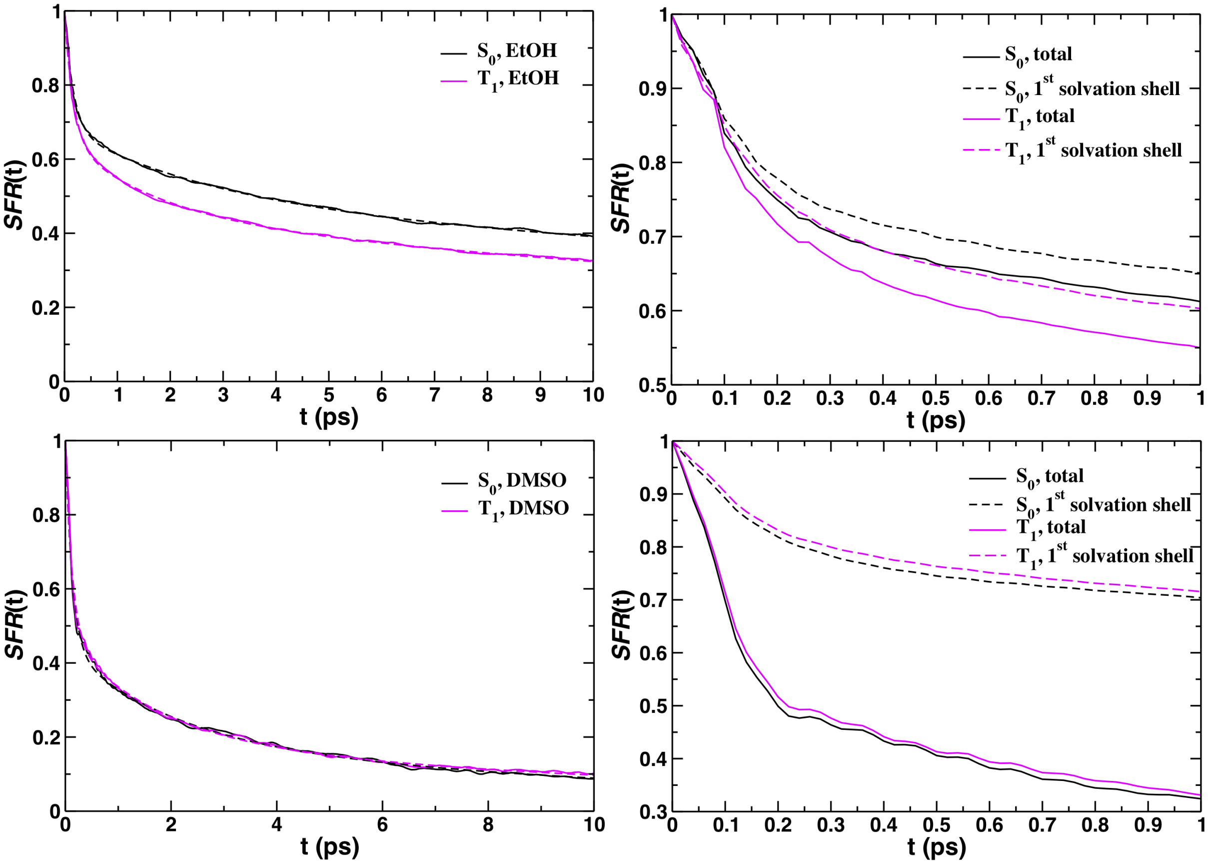

Figure 8: Solvation response function of ethanol (top panel) and of DMSO (bottom panel) in the equilibrium ground and T_1 excited state computed from MD simulations according to eq. (11). On the right side, the total *SRF*s are compared with the contributions arising from the first solvation shell on a shorter timescale.

response was observed in confined ethanol:[108] the local organization of solvent molecules in the confined systems results in a modified polarization field and thus a modified relaxation mechanism. In our case, the solute does not undergo a large dipolar excitation passing from the ground to the excited T_1 state but rather a significant change in the charge distribution, behaving similarly to a model benzene-like case proposed by Maroncelli and coworkers.[105] Moreover, contrarily to the cases discussed in the literature where the commonly employed probes show a strongly increased dipole moment in the excited state,[104] the value of the dipole moment in the ground state is slightly larger than the one in the excited state and, in addition, their relative orientations are quite similar, as shown in Figure C in Supporting Information. Using the equilibrium geometry and the partial charges of the employed QMD-FFs, we see that the solute molecular dipole decreases from 27.42 to 23.31 Debye from S_0 to T_1. This difference decreases when taking into account solvation and finite temperature effects, with the dipole distributions in the ground and excited state of Z907 that peak at 25.65 and 24.29 Debye, respectively (presented as Supporting Information, Figure E).

Turning to the *SRF* analysis, the results of the three-exponential fitting presented in equation (12) are reported in some detail in Table 2. The faster relaxation time τ_1 is associated with a contribution of about 30% of the total response and is practically identical for the ground and excited state responses. We can assume that this relaxation is related with the fast inertial part of the solvent reorganization, during which, the linear response holds.[104] The contribution due to the slowest relaxation time,τ_3, represents about 50% of the *SRF* in the case of the ground and of the excited state simulation. The two associated times are about 43 and 31 ps, respectively. The intermediate decay time τ_2 is more representative of time scales at which the solvent activates collective motions and it is more affected by the breakdown of the linear response approximation, leading to two different values from the ground and excited state simulations. The correlation time, computed by proper integration of the *SRF* according to equation (13) resulted to be 21.39 ps and 14.09 ps, for the ground and excited state response, respectively, to be compared with the experimental value 16 ps for coumarin.[105] However, in making the comparison with the C153 system, it is important to point out that it is now well established that the dynamics of the solvent is not only affected by its molecular and condensed phase properties,

	a_1	τ_1 (ps)	a_2	τ_2 (ps)	a_3	τ_3 (ps)	$< \tau >$ (ps)
EtOH, S_0	0.32	0.164	0.20	2.797	0.48	43.300	21.39
EtOH, T_1	0.35	0.163	0.21	1.731	0.44	31.074	14.09
DMSO, S_0	0.56	0.132	0.25	1.986	0.09	12.684	1.56
DMSO, T_1	0.52	0.129	0.28	1.686	0.10	14.382	1.98

Table 2: Results obtained by fitting the solvation response functions according to eq. (12) to the (normalized) linear combination of three exponential functions, and average correlation times (eq. 13).

but that the solute structure and internal motions can strongly influence such dynamics, even in the case of a fast rotating solvent such as water (see Refs. [109, 110] and references therein) and it was confirmed in ethanol and in dimethyl sulfoxide by recent experiments.[111]

When restricting the calculation of the *SRF* to the EtOH molecules in the first solvation shell, we found quite revealing results, reported in the top right panel of Figure 8. For times shorter than 100 fs, the *SRF*s decay at a very similar rate, whereas on a longer time scale the first solvation shell functions and the corresponding total functions display very different features, and the responses in the ground and in the excited state strongly differ. Librations in ethanol occur with a period of about 50 fs.[112] It is thus reasonable to assume that the inertial reorganization of the solvent takes place on time scale shorter than a 100 fs, and that more collective motions, which are sensitive to the different organization of the solvent around the solute, gain energy on a longer time scale. Unlike our case, for other systems in which the breakdown of linear response was observed, a faster solvent response was computed around the excited state solute compared with the ground state.[103, 104] In those cases, however, the solute-solvent local interactions were enhanced upon excitation, and the population of the first solvation shell increased as a consequence of the solute perturbation. On the contrary, our results of the solvation shells in ethanol point to a situation in which the first solvation shell is more populated around the solute in the S_0 state compared to T_1. As shown in the top left panel of Figure 7, on the one hand the solvent molecules in the first solvation shell of Z907 are affected by a remarkable weakening of the hydrogen bond interactions around the thiocyanate groups, corresponding to an important decrease in the number of HBs (Table 1) and to changes that propagate to the second solvation shell. On the other hand, the increased solute-solvent interactions around the carboxylic groups (middle left panels of Figure 7) are more localized, since they only affect the first peak of the radial distribution function, and the total number of HBs changes only slightly, as already noted. Comparing our trend with those in the literature, one can infer that a faster response seems to be related with strengthened local solute-solvent interactions.

Turning to DMSO, it is worth pointing out that the distributions of molecular dipole moments in the ground and in the excited state peak at 24.45 and 25.18 Debye, respectively (Figure E in Supporting Information). We thus observed a very small increase of this quantity, whereas a decrease was observed in ethanol. The ground and excited state simulations in DMSO provide extremely close results for the time decay of the solvation response. As in the case of ethanol, the best fit was provided by a three exponential function described in equation (12), and the fitted parameters are reported in Table 2. Comparing the calculated decay with experimental data for the C153/DMSO system,[113] also reported as a three exponential fit of the experimental response, we found a quite good agreement. The correlation time, calculated through eq. (13), is 1.56 ps for the ground state response and 1.98 ps for the excited state response, to be compared with 2 ps in experiments[105] and with 0.80 ps in non-equilibrium molecular dynamics simulations[114] of C153 in DMSO. As in our case, the local structure of the solvent around the ground and the excited state coumarin is very similar and it has been shown that the predicted non-equilibrium response of DMSO after electronic excitation of C153 is in agreement with the ground and excited state responses.[111,114] As a matter of fact, when calculating the response of the first shell solvent molecules, we obtained a remarkably different behavior compared with ethanol in a ps time scale. Results are displayed in the bottom right panel of Figure 8. The partial responses in the ground and in the excited state are very similar to each other but completely different with respect to the total response, even at a very short time scale. Since the very early stages of the solvent relaxation, the excess energy is thus transferred to farther solvation shells and the dynamics of the first shell molecules does not follow the same mechanism as the total response. This is consistent with the larger contribution given by the fast exponential (with decay time τ_1) to the total response compared to the case of ethanol (*cf.* the values of a_1 in Table 2). By Fourier transforming the *SRF*, we found that the weak oscillations that are present in the short time scale are related with motions occurring with frequencies of 54 cm^{-1} and of 107 cm^{-1}, which we can safely assign to librations.[115]

The picture of the different local interactions that we were able to present based on our MD simulations has allowed us to discuss some relevant features regarding the organization of solvent molecules around the ground and excited state solute, and how this organization may affect the solvent dynamic response for the two considered solvation media. In the following Section, we turn to analyze how these properties affect the solute electronic spectrum and to propose an interpretation of the comparison with the experimental measurements.

3.3 Dynamical and environmental effects on the steady-state absorption

We have already discussed the quality of our QMD-FF in section 3.1 on the basis of RMSDs, frequencies and relaxed scan profiles of selected dihedrals for both the QM and QMD-FF optimized S_0 and T_1 geometries. Here we start by comparing, in Figure 9, the calculated absorption spectra in implicit solvent (EtOH) for the two optimized S_0 structures, while in Table 3 a detailed characterization of the most intense transitions underlying the main peaks and shoulders of the absorption spectrum profile is reported. This characterization is based on the analysis of the unrelaxed one-electron transition density matrix[116,117] partitioned on the metal and ligands fragments, as implemented in the TheoDore package.[101,102] For a visual inspection, the iso-density plots of the density difference between the considered excited states and ground state are also displayed in Figure 9.

The maximum of the visible band is centered at about 490 nm and presents two low-energy shoulders at around 600 and 750 nm, originated by the $S_0 \rightarrow S_3$ and $S_0 \rightarrow S_1$ transitions, respectively. As shown by the hole and electron localization in Table 3, this low-energy tail is given by LML′CT states with a net CT from the Ru-NCS to the BPY-COOH ligand, having an higher electron accepting capability with respect to the BPY-alkyl ligand. The nature of the states underlying the first band around 490-500 nm is of LML′CT type as well, with the main charge flow again toward the BPY-COOH but with a certain particle localization also on the BPY-alkyl ligand, as shown in Table 3 and in Figure 9, by the rather intense $S_0 \rightarrow S_5$ excitation. At higher energy (*ca.* 380 nm), a smaller LML′CT band appears in the spectrum,

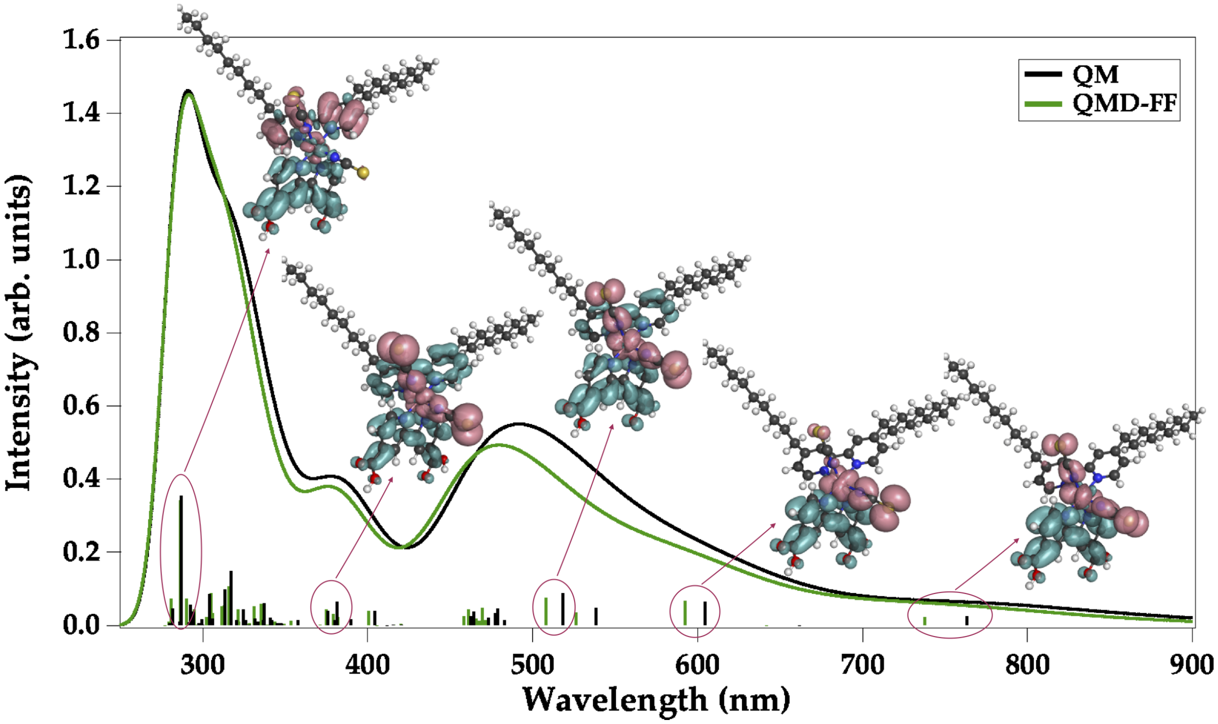

Figure 9: Calculated absorption spectra of Z907 in implicit EtOH on the QM (*vide infra*) and QMD-FF optimized geometries. The iso-density plots (iso-value 8.0×10^{-5}) of the density difference between the excited and the ground state associated to the most intense excitations are also plotted. Pink and cyan lobes indicates charge depletion and accumulation, respectively.

characterized by states in which the charge is mainly transferred from the NCS (74%), with a small contribution (12%) from the metal, to the two bypyridines (27% to BPY-COOH and 59% to BPY-alkyl). Finally, the highest-energy and most intense band is of inter-ligand (IL) nature, with mixed local (same ligand) and CT (different ligands) components: the hole is localized on the BPY-alkyl and NCS ligands for the 77 and 12%, respectively, while the particle on the BPY-alkyl and BPY-COOH for the 81 and 13%, respectively.

On the one hand, although the overall spectrum profile obtained from the two geometries is the same, still some appreciable differences appear on both position and intensity of the two visible LML′CT absorption bands. The maxima of the higher energy IL band are, on the other hand, perfectly overlapped. Concretely, only the lowest-energy MLCT band, computed for the QMD-FF optimized structure, presents a non negligible blue-shift (0.06 eV) and intensity decrease with respect to the QM reference. Since the discrepancies between the two spectra have to be related to the differences in the two geometries, this is a clear indication that they mostly concern the metal-ligand coordination. In fact, the elongation of the N(bpy)-Ru bond distances of about 0.02 Åobtained in the FF-optimized structure, seems to be sufficient to slightly reduce the charge density on the metal center and thus account for the slight shift at higher energies of the LML$'$CT states. Having discussed the accuracy of our QMD-FF with respect to the QM description and in light of the great sensitivity of the calculated optical properties to minimal

State	λ_{abs} (nm)	Fragment	*hole*	*particle*	CT
S_1	756	Ru	0.54	0.06	0.90
		NCS1	0.23	0.00	
		NCS2	0.13	0.00	
		BPY-COOH	0.06	0.89	
		BPY-alkyl	0.04	0.00	
S_3	604	Ru	0.41	0.08	0.89
		NCS1	0.42	0.01	
		NCS2	0.05	0.01	
		BPY-COOH	0.09	0.89	
		BPY-alkyl	0.03	0.02	
S_5	518	Ru	0.44	0.04	0.92
		NCS1	0.28	0.00	
		NCS2	0.18	0.01	
		BPY-COOH	0.06	0.75	
		BPY-alkyl	0.04	0.20	
S_{17}	381	Ru	0.17	0.05	0.95
		NCS1	0.32	0.00	
		NCS2	0.43	0.00	
		BPY-COOH	0.01	0.31	
		BPY-alkyl	0.00	0.63	
S_{45}	286	Ru	0.03	0.06	0.35
		NCS1	0.05	0.01	
		NCS2	0.14	0.00	
		BPY-COOH	0.01	0.13	
		BPY-alkyl	0.77	0.81	

Table 3: Nature and hole/particle localization of the most intense excitations giving rise to the absorption spectrum of Z907 in ethanol (QM-optimized geometry in Figure 9). The total CT associated with each transition is also reported.

changes in the Ru-ligand coordination geometry, the next questions are: "*how does the calculated spectrum on the optimized ground state geometry compare with the experimental one?*" and, above all, "*which is the role played by thermal, vibrational and solvation effects on the position and shape of the LML$'$CT bands?*"

As shown in the top panel of Figure 10 and by the corresponding maxima listed in Table 4, the spectrum recorded in ethanol (full black line) presents two main peaks in the 350-600 nm region, both traditionally assigned to LML$'$CT transitions. The lower-energy and narrower band has a maximum at 541 nm, while the second quite broadened band has the maximum absorption around 430 nm. A third strong IL bands appears in EtOH at 294 nm, as shown in Figure F in Supporting Information, where the static absorption spectra of Figure 9 are also plotted for the sake of comparison. As is apparent, while for the highest-energy IL bands, the calculated maximumum is predicted at 291 nm, essentially coinciding with the experimental one (Figure F in Supporting Information), for the LML$'$CT transitions, the experimental picture is dramatically different from the one obtained from the optimized gas-phase geometry (replotted as full-dotted magenta line in the top panel of Figure 10 for an easier visual comparison) where the two calculated bands have neither the correct intensity nor the correct position when compared to the experimental ones. Remarkably, when explicit/implicit solvation and finite temperature effects are taken into account (red full line), a low-energy band, centered at 557 nm and only 0.06 eV red-shifted with respect to the experimental maximum, appears. This band is mainly given by excitations from the Ru-NCS ligand toward the BPY-COOH moiety, gaining intensity in consequence of the symmetry breaking and of a partial hole delocalization on the BPY ligands.

Thermal motion and symmetry distortions also lower the energy of the Ru-NCS → BPY-alkyl excitations, resulting in a certain states mixing, and even states inversion, in this low-energy portion of the spectrum. The second calculated LML$'$CT band has a maximum at 470 nm, being more than 0.3 eV lower in energy with respect to the experimental maximum, and, above all, it does not present the broadened profile appearing in the experiments. We can, however, speculate that this second broad band might actually correspond to what we calculated as second (470 nm) and third ($\approx$ 380 nm) bands, with the latter clearly present in the "0 K"

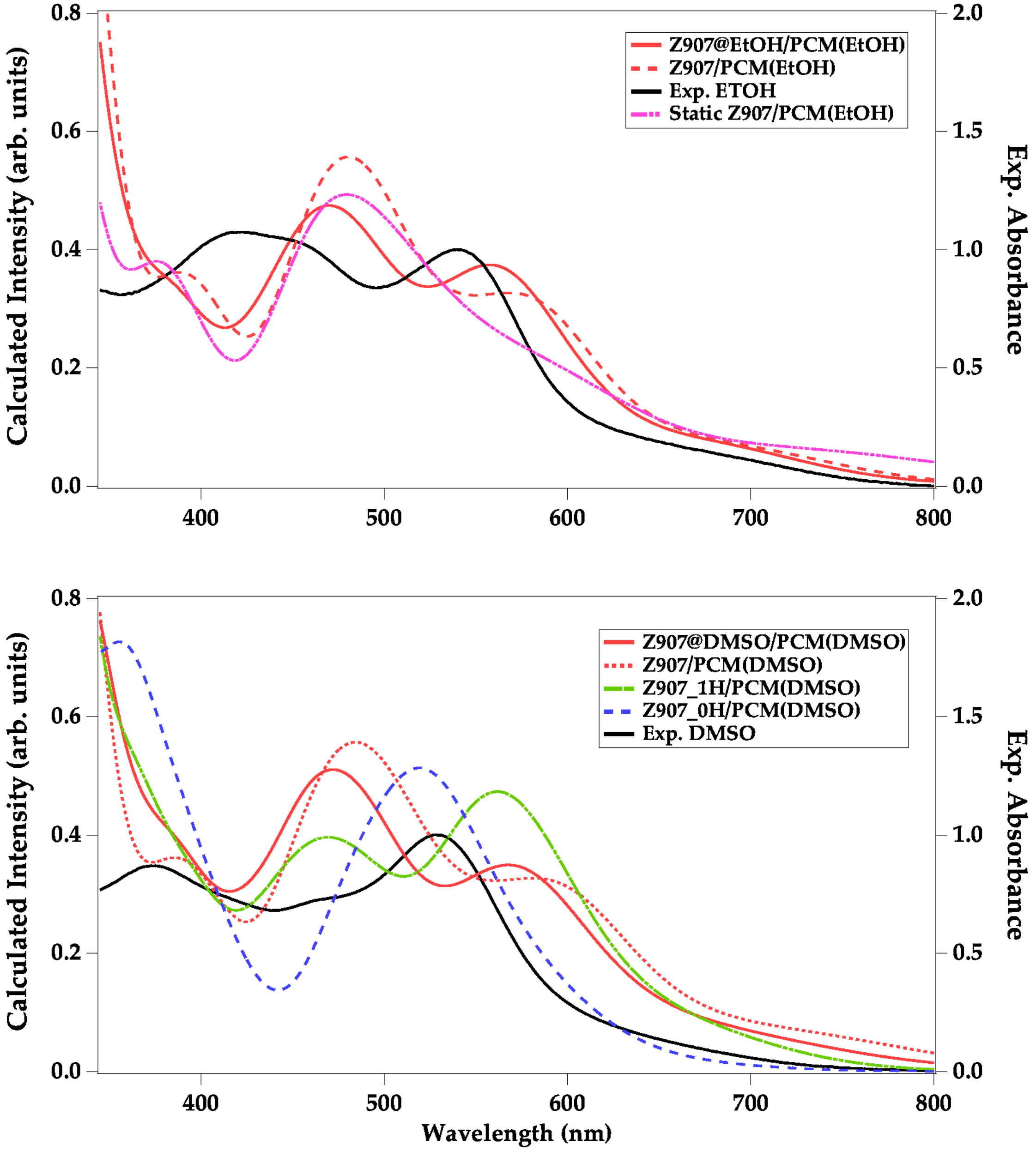

Figure 10: Calculated vs. experimental absorption spectra of Z907 in EtOH (top) and DMSO (bottom). Two different levels of treatment of the solvent are considered: 1) (full lines) the explicit/implicit hybrid scheme denoted as *Z907@solvent/PCM(solvent)*; 2) (dotted lines) the implicit scheme denoted as *Z907/PCM(solvent)*. In the case of DMSO the mono-deprotonated (1H) and fully deprotonated (0H) species are also simulated.

Solvent	Method	E_{max}, nm (eV)		
		I	II	III
EtOH	Z907@EtOH/PCM(EtOH)	557 (2.23)	470 (2.64)	-
	Z907/PCM(EtOH)	586 (2.12)	489 (2.54)	393 (3.26)
	Exp.	541 (2.29)	430 (2.88)	-
DMSO	Z907@DMSO/PCM(DMSO)	568 (2.19)	472 (2.63)	-
	Z907/PCM(DMSO)	581 (2.14)	484 (2.56)	385 (3.22)
	Z907_1H/PCM(DMSO)	562 (2.21)	469 (2.64)	-
	Z907_0H/PCM(DMSO)	519 (2.39)	355 (3.49)	-
	Exp.	530 (2.34)	370 (3.35)	-

Table 4: Calculated and experimental absorption maxima (in EtOH and DMSO) of Z907 in the 350-600 nm region. The maxima are given in nm, while eV values are reported within parenthesis.

spectra in Figure 9 and appearing as a shoulder of the IL band in the thermal averaged spectrum when the first shell of ethanol is explicitily considered (Z907@EtOH/PCM(EtOH), full red line). The role played by the two different descriptions adopted to take the solvent into account, deserves, indeed, some additional remarks. The lowest-energy band (dotted red line in Figure 10, Z907/PCM(EtOH)) is present in both cases, confirming that it is overall originated from structural fluctuations breaking the symmetry of the metal-ligands framework. Yet, a 0.1 eV red-shift is obtained when EtOH is described by a continuum, replacing all the solvent molecules in the MD snapshots. Considering explicit HBs provides, indeed, a more realistic ground state charge distribution, with less/more negative NCS/COOH groups. Moreover, a non negligible effect on the bands profile is also apparent, in particular, as discussed above, on the small peak at 380 nm.

Moving to the results obtained in DMSO (Table 4 and bottom panel of Figure 10), the spectrum calculated over the MD snapshots does not reproduce the 0.05 and 0.47 eV blue-shifts measured for the first and second bands, respectively. When the explicit/implicit solvation scheme is employed (red full line), indeed, the first and second band maxima are even slightly red-shifted by 0.04 and 0.01 eV, respectively, with respect to the ones calculated in EtOH. Predicting the solvato-chromism of Z907 in EtOH and DMSO is not straightforward, as the two solvents have a significantly different polarity ($\varepsilon \approx 25$ and 47 for ethanol and DMSO, respectively) and different HB interactions with the solute, as discussed in section 3.2. A TD-DFT calculation on the QM optimized geometry in C-PCM, predicts a small blue-shift from 482 to 479 nm (0.02 eV) going from EtOH to DMSO (see Figure G in Supporting Information), in line with the shift measured for the lowest-energy band. When, however, one considers a "microsolvation plus implicit" scheme', with 4 solvent molecules (2 interacting with the COOH groups and 2 with the NCS ligands) in C-PCM, a small red-shift from 454 to 458 nm (0.02 eV) going from EtOH to DMSO is predicted (Figure E in Supporting Information), possibly caused by the destabilization of the LML′CT states due to the H-bonds formed between the NCS ligands and the solvent, compensating the shift at higher energies due to the higher solvent polarity. In any case, in the experimental spectra, the effect on both the position and profile of the second band going from EtOH to DMSO is considerable and, above all, it seems to be completely missed by the simulations.

The lacks found in the spectra computed in DMSO were rather unexpected, especially considering the above considerations on the role of the solvent and the fact that the same intramolecular QMD-FF for the solute was employed EtOH simulations, where a nice agreement with the experiment was found. An explanation for such a large shift should be therefore searched in the possible co-existence of various protonation states of the solute in DMSO, caused by its strong nucleophilic properties,[118] inducing deprotonation of the carboxylic groups. Such deprotonated species were not taken into account in our model, and their lack could explain the different performances in the two solvents. To substantiate this interpretation, we calculated the thermal averaged absorption spectra in implicit DMSO for the fully protonated (Z907), mono-deprotonated (Z907_1H) and fully deprotonated (Z907_0H) forms (dotted red, green and blue lines in the bottom panel of Figure 10, respectively). To simulate the 1H/0H Z907 species, we removed 1/2 carboxylic protons from the MD snapshots, replacing all the solvent molecules with the C-PCM. This is clearly a rough approximation to the actual deprotonation process in solution, that cannot be described with classical simulation methods, not allowing for the solute's protons to be partially/totally transferred to the solvent. Comparing the three spectra and the nature of the transitions underlying the main bands, however, is useful to quantify and interpret the spectral shift due to deprotonation effects. The spectrum of the protonated Z907 in

DMSO, in agreement with that calculated in EtOH, presents three maxima in the 350-600 nm range, at 581, 484 and 385 nm (Table 4), with the nature of the excited states discussed above. When one of the carboxylic group is deprotonated, a blue-shift (0.07 and 0.08 eV) along with a reversal of intensity of the two lowest-energy bands is predicted; the small band at 385 nm disappears. Fully deprotonation (Z907_0H) yields, as expected, a larger shift (0.25 eV on the first band with respect to the fully protonated form) and a pronounced spectral reshaping (Figure 10). A deeper look at the excited states nature discloses that monodeprotonation, destabilizing the BPY-COOH molecular orbitals, induces a blue shift in both the lowest energy band, whose intensity is mainly given by Ru-NCS→BPY-COOH excitations, and the second band (470 nm), where mixed Ru-NCS→BPY-COOH and Ru-NCS→BPY-alkyl states appear. Deprotonation of the second carboxylic group makes Ru-NCS→BPY-COO^{2-} and Ru-NCS→BPY-alkyl states almost degenerate, in such a way that under the intense and broad band at 2.39 eV a complex mixing of excitations from the Ru-NCS toward the two BPY ligands along with local $\pi \rightarrow \pi^*$ excitations on the BPY-COO^{2-} ligand are present. The higher energy peak (ca. 350 nm) is still given by mixed excitations, with a more definite IL nature. The hypothesis of a mixture of different degrees of protonation in DMSO might, thus, explain the observed spectral reshaping and blue-shift, that, as we discussed above, cannot be reproduced on the fully protonated Z907, even when an hybrid explicit/implicit solvent description is adopted.

4 Conclusions

By combining classical MD simulations based on quantum-mechanically derived FFs, specifically parameterized for the target system, linear response analysis of the solvent dynamics and large scale TD-DFT excited states calculations, we report here an unprecedented computational study on the solvation and dynamical effects on the optical absorption spectroscopy of a prototype heteroleptic Ru(II) polypyridyl complex commonly employed in DSSCs.

A polar protic (ethanol) and a strong nucleophilic aprotic (dimethyl sulfoxyde) solvent are considered in virtue of their different hydrogen-bonding formation capabilities and of their different response to the electronic CT excitation.[30] To overcome the well known deficiencies of standard force-fields in the description of both the octahedral symmetry of the metal-ligand framework and the absence of proper parameters to represent the triplet state, we resorted to a quantum-mechanical derivation of the FF parameters, specifically carried out for the target systems. The resulting FF was thereafter employed in extensive MD simulations, to reliably sample the conformational space explored by the solute-solvent systems in ambient conditions and to gain a deeper insight into the microscopic solvation structure.

Analysis of the solvent relaxation dynamics in the ground, S_0, and excited triplet state, T_1, discloses, indeed, that in the protic solvent, the significant hydrogen-bonds rearrangement upon the electronic excitation is responsible for the breakdown of the linear response approximation.[106] Such a breakdown is well known, and several groups have provided an interpretation based on the analysis of the modified ordering within the solvent, induced by the solute excitation.[103,104] In particular, in line with the recent results reported by Heid et al.,[106] our findings show that the the LR approximation breakdown is induced by important structural changes in the HB network of the first solvation shell, following the sudden electronic distribution rearrangement of the solute. Structural reorganizations between the first and second solvation shell are, indeed, observed in the Ru-NCS region as a consequence of the net charge depletion in the triplet state, leading to a marked depopulation/population in the former/latter. The linear response regime holds, instead, in DMSO where the H-bond interactions with the OH groups are essentially unaffected by the change of the electronic distribution and the excess energy is promptly transferred to farther solvent molecules.

Concerning the optical response, the different solute-solvent interactions taking place in the two environments and the finite temperature effect were also found to be crucial when comparing the calculated absorption spectra with the experimental ones. In fact, in ethanol, the inclusion of dynamical effects and the use of a proper hybrid explicit/implicit solvation model have been shown to be mandatory to reproduce the overall shape and position of the two lowest-energy absorption bands appearing in the experimental spectrum, whereas the static “0 K” DFT picture, that is routinely applied for the excited states calculations of these systems, was found to be unable to provide a reliable prediction of the experimental spectral profile. Interesting insights also come from the simulations in DMSO, where it was impossible to reproduce the appreciable blue shift measured for the two LML′CT bands with respect to the ones appearing in EtOH, even when the first solvent shell is explicitely included. By modeling at DFT level of theory the spectral shifts originated by including an explicit micro-solvation shell and the optical response associated to the mono-deprotonated and fully deprotonated forms of the solute, we suggest that the solvatochromic shift and the spectrum reshaping in DMSO could actually to be attributed to the co-existence of different deprotonated forms, which are stabilized in the strongly nucleophilic DMSO solvent but not accounted for in our non-reactive MD framework.

Finally, it is worth pointing out that the multilevel approach here proposed can be generalized to any transition metal coordination complex and to any electronic state, overcoming the limitations due to the lack of standard force fields to correctly reproduce the octahedral coordination, and opening the way to the simulation of transient absorption spectroscopies.

Supporting Information

Additional details on intra- and inter-molecular parameterization, including a complete list of the employed FF parameters. Supplementary charge and dipole analysis. Conformational and dipole distributions achieved in MD simulations and steady-state absorption spectra. Specific input and output files of the several codes employed throughout the present work are available from the authors upon request.

Acknowledgments MP thanks *ANR JCJC HELIOSH2* (ANR-17-CE05-0007-01) for financial support and HPC resources from GENCI-CCRT/CINES (Grants 2018-A0010810139).

References

[1] Listorti, A.; Durrant, J.; Barber, J. Solar to fuel *Nature Mater.* **2009**, *8*, 929–930.

[2] Sension, R. J. Quantum path to photosynthesis *Nature* **2007**, *446*, 740–741.

[3] Jailaubekov, A. E.; Willard, A. P.; Tritsch, J. R.; Chan, W.-L.; Sai, N.; Gearba, R.; Kaake, L. G.; Williams, K. J.; Leung, K.; Rossky, P. J.; Zhu, X.-Y. Hot charge-transfer excitons set the time limit for charge separation at donor/acceptor interfaces in organic photovoltaics *Nature Mater.* **2013**, *12*, 66–73.

[4] Grätzel, M. Conversion of sunlight to electric power by nanocrystalline dye-sensitized solar cells *J. Photochem. Photobiol. A* **2004**, *164*, 3–14.

[5] Zhang, M.; Murakami, T.; Ajima, K.; Tsuchida, K.; Sandanayaka, A. S. D.; Ito, O.; Iijima, S.; Yudasaka, M. Fabrication of ZnPc/protein nanohorns for double photodynamic and hyperthermic cancer phototherapy. *PNAS* **2008**, *105*, 14773–8.

[6] Cheng, L.; Wang, C.; Feng, L.; Yang, K.; Liu, Z. Functional Nanomaterials for Phototherapies of Cancer *Chem. Rev.* **2014**, *114*, 10869–10939.

[7] Crosby, G. A.; Perkins, W. G.; Klassen, D. M. Luminescence from TransitionMetal Complexes: Tris(2,2bipyridine) and Tris(1,10phenanthroline)Ruthenium(II) *J. Chem. Phys.* **1965**, *43*, 1498–1503.

[8] Gafney, H. D.; Adamson, A. W. Excited state Ru(bipyr)32+ as an electron-transfer reductant *J. Am. Chem. Soc.* **1972**, *94*, 8238–8239.

[9] Sabbatini, N.; Balzani, V. Photosensitized aquation of the hexacyanochromate(III) ion. Evidence against the doublet mechaism *J. Am. Chem. Soc.* **1972**, *94*, 7587–7589.

[10] Bock, C. R.; Meyer, T. J.; Whitten, D. G. Electron transfer quenching of the luminescent excited state of tris(2,2'-bipyridine)ruthenium(II). Flash photolysis relaxation technique for measuring the rates of very rapid electron transfer reactions *J. Am. Chem. Soc.* **1974**, *96*, 4710–4712.

[11] Grätzel, M. Artificial photosynthesis: water cleavage into hydrogen and oxygen by visible light *Acc. Chem. Res.* **1981**, *14*, 376–384.

[12] Ghosh, P.; Spiro, T. G. Photoelectrochemistry of tris(bipyridyl)ruthenium(II) covalently attached to n-type tin(IV) oxide *J. Am. Chem. Soc.* **1980**, *102*, 5543–5549.

[13] Nazeeruddin, M. K.; Kay, A.; Rodicio, I.; Humphry-Baker, R.; Mueller, E.; Liska, P.; Vlachopoulos, N.; Grätzel, M. Conversion of light to electricity by cis-X2bis(2,2'-bipyridyl-4,4'-dicarboxylate)ruthenium(II) charge-transfer sensitizers (X = Cl-, Br-, I-,

CN-, and SCN-) on nanocrystalline titanium dioxide electrodes *J. Am. Chem. Soc.* **1993**, *115*, 6382–6390.

[14] Nazeeruddin, M. K.; De Angelis, F.; Fantacci, S.; Selloni, A.; Viscardi, G.; Liska, P.; Ito, S.; Takeru, B.; Grätzel, M. Combined Experimental and DFT-TDDFT Computational Study of Photoelectrochemical Cell Ruthenium Sensitizers *J. Am. Chem. Soc.* **2005**, *127*, 16835–16847.

[15] Nazeeruddin, M. K.; Péchy, P.; Grätzel, M. Efficient panchromatic sensitization of nanocrystalline TiO2 films by a black dye based on a trithiocyanatoruthenium complex *Chem. Comm.* **1997**, *0*, 1705–1706.

[16] Nazeeruddin, M. K.; Péchy, P.; Renouard, T.; Zakeeruddin, S. M.; Humphry-Baker, R.; Comte, P.; Liska, P.; Cevey, L.; Costa, E.; Shklover, V.; Spiccia, L.; Deacon, G. B.; Bignozzi, C. A.; Grätzel, M. Engineering of Efficient Panchromatic Sensitizers for Nanocrystalline TiO2-Based Solar Cells *J. Am. Chem. Soc.* **2001**, *123*, 1613–1624.

[17] Pastore, M.; De Angelis, F. In *Multiscale Modelling of Organic and Hybrid Photovoltaics*; Beljonne, D.; Cornil, J., Eds.; Springer Berlin Heidelberg: Berlin, Heidelberg, 2014; pp 151–236.

[18] Pastore, M.; Selloni, A.; Fantacci, S.; De Angelis, F. In *Electronic and Optical Properties of Dye-Sensitized TiO2 Interfaces*; Springer, Berlin, Heidelberg, 2014; pp 1–45.

[19] Chen, P.; Meyer, T. J. Medium Effects on Charge Transfer in Metal Complexes *Chem. Rev.* **1998**, *98*, 1439–1478.

[20] Damrauer, N. H.; Cerullo, C. V.; Yeh, J. K.; Boussie; Shank; McCusker Femtosecond Dynamics of Excited-State Evolution in *Science* **1997**, *275*, 54–7.

[21] Heitele, H. Dynamic Solvent Effects on Electron-Transfer Reactions *Angew. Chem. Int. Ed.* **1993**, *32*, 359–377.

[22] Onfelt, B.; Lincoln, P.; Nordén, B.; Baskin, J. S.; Zewail, A. H. Femtosecond linear dichroism of DNA-intercalating chromophores: solvation and charge separation dynamics of [Ru(phen)2dppz]2+ systems. *Proc. Natl. Acad. Sci. USA* **2000**, *97*, 5708–13.

[23] Bhasikuttan, A. C.; Suzuki, M.; Nakashima, S.; Okada, T. Ultrafast Fluorescence Detection in Tris(2,2-bipyridine)ruthenium(II) Complex in Solution: Relaxation Dynamics Involving Higher Excited States *J. Am. Chem. Soc.* **2002**, *124*, 8398–8405.

[24] Wallin, S.; Davidsson, J.; Modin, J.; Hammarström, L. Femtosecond Transient Absorption Anisotropy Study on [Ru(bpy)3]2+ and [Ru(bpy)(py)4]2+. Ultrafast Interligand Randomization of the MLCT State *J. Phys. Chem. A* **2005**, *109*, 4697–4704.

[25] Rondi, A.; Rodriguez, Y.; Feurer, T.; Cannizzo, A. Solvation-Driven Charge Transfer and Localization in Metal Complexes *Acc. Chem. Res.* **2015**, *48*, 1432–1440.

[26] Moret, M.-E.; Tavernelli, I.; Rothlisberger, U. Combined QM/MM and Classical Molecular Dynamics Study of [Ru(bpy)3]2+ in Water *J. Phys. Chem. B* **2009**, *113*, 7737–7744.

[27] Moret, M.-E.; Tavernelli, I.; Chergui, M.; Rothlisberger, U. Electron Localization Dynamics in the Triplet Excited State of [Ru(bpy)3]2+ in Aqueous Solution *Chem. Eur. J.* **2010**, *16*, 5889–5894.

[28] Tomasi, J.; Mennucci, B.; Cammi, R. Quantum Mechanical Continuum Solvation Models *Chem. Rev.* **2005**, *105*, 2999–3094.

[29] Marotta, G.; Lobello, M. G.; Anselmi, C.; Barozzino Consiglio, G.; Calamante, M.; Mordini, A.; Pastore, M.; De Angelis, F. An Integrated Experimental and Theoretical Approach to the Spectroscopy of Organic-Dye-Sensitized TiO2 Heterointerfaces: Disentangling the Effects of Aggregation, Solvation, and Surface Protonation *ChemPhysChem* **2013**, *15*, 1116–1125.

[30] Azzaroli, N.; Lobello, M. G.; Lapini, A.; Iagatti, A.; Bussotti, L.; Di Donato, M.; Calogero, G.; Pastore, M.; De Angelis, F.; Foggi, P. Monitoring the intramolecular charge

transfer process in the Z907 solar cell sensitizer: a transient Vis and IR spectroscopy and ab initio investigation *Phys. Chem. Chem. Phys.* **2015**, *17*, 21594–21604.

[31] Mosconi, E.; Azpiroz, J. M.; De Angelis, F. Ab Initio Molecular Dynamics Simulations of Methylammonium Lead Iodide Perovskite Degradation by Water *Chem. Mater.* **2015**, *27*, 4885–4892.

[32] Piccinin, S.; Rocca, D.; Pastore, M. Role of Solvent in the Energy Level Alignment of Dye-Sensitized NiO Interfaces *J. Phys. Chem. C* **2017**, *121*, 22286–22294.

[33] Laio, A.; VandeVondele, J.; Rothlisberger, U. A Hamiltonian electrostatic coupling scheme for hybrid CarParrinello molecular dynamics simulations *J. Chem. Phys.* **2002**, *116*, 6941–6947.

[34] Senn, H. M.; Thiel, W. QM/MM Methods for Biomolecular Systems *Angew. Chem. Int. Ed.* **2009**, *48*, 1198–1229.

[35] Loco, D.; Polack, E.; Caprasecca, S.; Lagardère, L.; Lipparini, F.; Piquemal, J.-P.; Mennucci, B. A QM/MM Approach Using the AMOEBA Polarizable Embedding: From Ground State Energies to Electronic Excitations *J. Chem. Theory Comput.* **2016**, *12*, 3654–3661.

[36] Morzan, U. N.; Alonso de Armino, D. J.; Foglia, N. O.; Ramírez, F.; González Lebrero, M. C.; Scherlis, D. A.; Estrin, D. A. Spectroscopy in Complex Environments from QMMM Simulations *Chem. Rev.* **2018**, *118*, 4071–4113.

[37] Allen, M. P.; Tildesley, D. J. Computer Simulation of Liquids; Clarendon: Oxford, 1987.

[38] Frenkel, D.; Smith, B. Understanding Molecular Simulations; Academic Press: San Diego, 1996.

[39] Jorgensen, W. L.; Tirado-Rives, J. Potential Energy Functions for Atomic-Level Simulations of Water and Organic and Biomolecular Systems. *Proc. Natl. Acad. Sci. USA* **2005**, *102*, 6665–70.

[40] Caleman, C.; van Maaren, P. J.; Hong, M.; Hub, J. S.; Costa, L. T.; van der Spoel, D. Force Field Benchmark of Organic Liquids: Density, Enthalpy of Vaporization, Heat Capacities, Surface Tension, Isothermal Compressibility, Volumetric Expansion Coefficient, and Dielectric Constant *J. Chem. Theory Comput.* **2012**, *8*, 61–74.

[41] Li, J.; Lakshminarayanan, R.; Bai, Y.; Liu, S.; Zhou, L.; Pervushin, K.; Verma, C.; Beuerman, R. W. Molecular Dynamics Simulations of a New Branched Antimicrobial Peptide: a Comparison of Force Fields. *J. Chem. Phys.* **2012**, *137*, 215101.

[42] Cui, S.; de Almeida, V. F.; Hay, B. P.; Ye, X.; Khomami, B. Molecular Dynamics Simulation of Tri-n-Butyl-Phosphate Liquid: a Force Field Comparative Study. *J. Phys. Chem. B* **2012**, *116*, 305–13.

[43] Jahn, D. A.; Akinkunmi, F. O.; Giovambattista, N. Effects of Temperature on the Properties of Glycerol: A Computer Simulation Study of Five Different Force Fields. *J. Phys. Chem. B* **2014**, *118*, 11284–11294.

[44] Prampolini, G.; Livotto, P. R.; Cacelli, I. Accuracy of Quantum Mechanically Derived Force-Fields Parameterized from Dispersion-Corrected DFT Data: The Benzene Dimer as a Prototype for Aromatic Interactions. *J. Chem. Theory Comput.* **2015**, *11*, 5182–96.

[45] Fischer, N. M.; van Maaren, P. J.; Ditz, J. C.; Yildirim, A.; van der Spoel, D. Properties of Organic Liquids when Simulated with Long-Range Lennard-Jones Interactions *J. Chem. Theory Comput.* **2015**, *11*, 2938–2944.

[46] Cerezo, J.; Santoro, F.; Prampolini, G. Comparing classical approaches with empirical or quantum-mechanically derived force fields for the simulation electronic lineshapes: application to coumarin dyes *Theor. Chem. Accounts* **2016**, *135*, 143.

[47] Andreussi, O.; Prandi, I. G.; Campetella, M.; Prampolini, G.; Mennucci, B. Classical Force Fields Tailored for QM Applications: Is It Really a Feasible Strategy? *J. Chem. Theory Comput.* **2017**, *13*, 4636–4648.

[48] Mennucci, B. Modeling absorption and fluorescence solvatochromism with QM/Classical approaches *Int. J. Quant. Chem.* **2015**, *18*, 1202–1208.

[49] Vaiana, A.; Schulz, A.; Wolfrum, J.; Saure, M.; Smith, J. Molecular Mechanics Force Field Parameterization of the Fluorescent Probe Rhodamine 6G Using Automated Frequency Matching *J. Comp. Chem.* **2003**, *24*, 632–639.

[50] Cournia, Z.; Vaiana, A.; Matthias Ulmann, G.; Smith, J. Derivation of a Molecular Mechanics Force Field for Cholesterol *Pure Appl. Chem.* **2004**, *76*, 189–196.

[51] Cacelli, I.; Prampolini, G. Parametrization and Validation of Intramolecular Force Fields Derived from DFT Calculations *J. Chem. Theory Comput.* **2007**, *3*, 1803–1817.

[52] Verstraelen, T.; Van Neck, D.; Ayers, P.; Van Speybroek, V.; Waroquier, M. The Gradient Curves Method: An Improved Strategy for the Derivation of Molecular Mechanics Valence Force Fields from ab Initio Data *J. Chem. Theory Comput.* **2007**, *3*, 1420–1434.

[53] Waldher, B.; Kuta, J.; Chen, S.; Henson, N.; Clark, A. ForceFit: A Code to Fit Classical Force Fields to Quantum Mechanical Potential Energy Surfaces *J. Comp. Chem.* **2010**, *31*, 2307–2316.

[54] Barone, V.; Cacelli, I.; De Mitri, N.; Licari, D.; Monti, S.; Prampolini, G. Joyce and Ulysses: Integrated and User-Friendly Tools for the Parameterization of Intramolecular Force Fields from Quantum Mechanical Data. *Phys. Chem. Chem. Phys.* **2013**, *15*, 3736–51.

[55] Akin-Ojo, O.; Song, Y.; Wang, F. Developing *ab initio* quality force fields from condensed phase quantum-mechanics/molecular -mechanics calculations through the adaptive force matching method *J. Chem. Phys.* **2008**, *129*, 64108.

[56] Cacelli, I.; Lami, C. F.; Prampolini, G. Force-field Modeling through Quantum Mechanical Calculations: Molecular Dynamics Simulations of a Nematogenic Molecule in its Condensed Phases. *J. Comp. Chem.* **2009**, *30*, 366–378.

[57] Piquemal, J.-P.; Jordan, K. D. From Quantum Mechanics to Force Fields: New Methodologies for the Classical Simulation of Complex Systems *Theor. Chem. Accounts* **2012**, *131*, 1207.

[58] Cacelli, I.; Cimoli, A.; Livotto, P. R.; Prampolini, G. An Automated Approach for the Parameterization of Accurate Intermolecular Force-Fields: Pyridine as a Case Study. *J. Comp. Chem.* **2012**, *33*, 1055.

[59] Grimme, S. A General Quantum Mechanically Derived Force Field (QMDFF) for Molecules and Condensed Phase Simulations *J. Chem. Theory Comput.* **2014**, 4497–4514.

[60] Vanduyfhuys, L.; Vandenbrande, S.; Verstraelen, T.; Schmid, R.; Waroquier, M.; Van Speybroeck, V. QuickFF: A Program for a Quick and Easy Derivation of Force Fields for Metal-Organic Frameworks from Ab Initio Input. *J. Chem. Theory Comput.* **2015**, *36*, 1015–27.

[61] Madarász, Á.; Berta, D.; Paton, R. S. Development of a True Transition State Force Field from Quantum Mechanical Calculations *J. Chem. Theory Comput.* **2016**, *12*, 1833–1844.

[62] Cisneros, G. A.; Wikfeldt, K. T.; Ojamäe, L.; Lu, J.; Xu, Y.; Torabifard, H.; Bartók, A. P.; Csányi, G.; Molinero, V.; Paesani, F. Modeling Molecular Interactions in Water: From Pairwise to Many-Body Potential Energy Functions *Chem. Rev.* **2016**, *116*, 7501–7528.

[63] Prampolini, G.; Campetella, M.; De Mitri, N.; Livotto, P. R.; Cacelli, I. Systematic and Automated Development of Quantum Mechanically Derived Force Fields: The Challenging Case of Halogenated Hydrocarbons *J. Chem. Theory Comput.* **2016**, *12*, 5525–5540.

[64] Paesani, F. Getting the Right Answers for the Right Reasons: Toward Predictive Molecular Simulations of Water with Many-Body Potential Energy Functions *Acc. Chem. Res.* **2016**, *49*, 1844–1851.

[65] Piquemal, J.-p.; Jordan, K. D. Preface: Special Topic: From Quantum Mechanics to Force Fields *J. Chem. Phys.* **2017**, *147*, 161401.

[66] Zahariev, F.; De Silva, N.; Gordon, M. S.; Windus, T. L.; Dick-Perez, M. ParFit: A Python-Based Object-Oriented Program for Fitting Molecular Mechanics Parameters to ab Initio Data *J. Chem. Inf. Mod.* **2017**, *57*, 391–396.

[67] Cerezo, J.; Prampolini, G.; Cacelli, I. Developing accurate intramolecular force fields for conjugated systems through explicit coupling terms *Theor. Chem. Accounts* **2018**, *137*, 80.

[68] Prampolini, G.; Yu, P.; Pizzanelli, S.; Cacelli, I.; Yang, F.; Zhao, J.; Wang, J. Structure and Dynamics of Ferrocyanide and Ferricyanide Anions in Water and Heavy Water: An Insight by MD Simulations and 2D IR Spectroscopy *J. Phys. Chem. B* **2014**, *118*, 14899–14912.

[69] Barone, V.; Bloino, J.; Monti, S.; Pedone, A.; Prampolini, G. Theoretical multilevel approach for studying the photophysical properties of organic dyes in solution. *Phys. Chem. Chem. Phys.* **2010**, *12*, 10550–61.

[70] De Mitri, N.; Monti, S.; Prampolini, G.; Barone, V. Absorption and Emission Spectra of a Flexible Dye in Solution: A Computational Time-Dependent Approach *J. Chem. Theory Comput.* **2013**, *9*, 4507–4516.

[71] Cacelli, I.; Ferretti, A.; Prampolini, G. Predicting light absorption properties of anthocyanidins in solution: a multi-level computational approach *Theor. Chem. Accounts* **2016**, *135*, 156.

[72] Del Galdo, S.; Mancini, G.; Daidone, I.; Polzi, L. Z.; Amadei, A.; Barone, V. Tyrosine absorption spectroscopy: Backbone protonation effects on the side chain electronic properties *J. Comp. Chem.* **2018**, *39*, 1747–1756.

[73] Giovannini, T.; Del Frate, G.; Lafiosca, P.; Cappelli, C. Effective computational route towards vibrational optical activity spectra of chiral molecules in aqueous solution *Phys. Chem. Chem. Phys.* **2018**, *20*, 9181–9197.

[74] Pedone, A.; Prampolini, G.; Monti, S.; Barone, V. Realistic Modeling of Fluorescent Dye-Doped Silica Nanoparticles: A Step Toward the Understanding of their Enhanced Photophysical Properties. *Chem. Mater.* **2011**, *23*, 5016–5023.

[75] Prampolini, G.; Monti, S.; De Mitri, N.; Barone, V. Evidences of long lived cages in functionalized polymers: Effects on chromophore dynamic and spectroscopic properties *Chem. Phys. Lett.* **2014**, *601*, 134–138.

[76] De Mitri, N.; Prampolini, G.; Monti, S.; Barone, V. Structural, dynamic and photophysical properties of a fluorescent dye incorporated in an amorphous hydrophobic polymer bundle. *Phys. Chem. Chem. Phys.* **2014**, *16*, 16573–87.

[77] Chantzis, A.; Very, T.; Monari, A.; Assfeld, X. Improved Treatment of Surrounding Effects: UV/vis Absorption Properties of a Solvated Ru(II) Complex *J. Chem. Theory Comput.* **2012**, *8*, 1536–1541.

[78] Tomasi, J.; Mennucci, B.; Cammi, R. Quantum Mechanical Continuum Solvation Models *Chem. Rev.* **2005**, *105*, 4708.

[79] Frisch, M. J.; Trucks, G. W.; Schlegel, H. B.; Scuseria, G. E.; Robb, M. A.; Cheeseman, J. R.; Scalmani, G.; Barone, V.; Mennucci, B.; Petersson, G.; Nakatsuji, H.; Caricato, M.; Li, X.; Hratchian, H. P.; Izmaylov, A. F.; Bloino, J.; Zheng, G.; Sonnenberg, J. L.; Hada, M.; Ehara, M.; Toyota, K.; Fukuda, R.; Hasegawa, J.; Ishida, M.; Nakajima, T.; Honda, Y.; Kitao, O.; Nakai, H.; Vreven, T.; Montgomery, J. A.; Peralta, J. E.; Ogliaro, F.; Bearpark, M.; Heyd, J. J.; Brothers, E.; Kudin, K. N.; Staroverov, V. N.; Kobayashi, R.; Normand, J.; Raghavachari, K.; Rendell, A.; Burant, J.; Iyengar, S. S.; Tomasi, J.; ; Cossi, M.; Rega, N.; Millam, J. M.; Klene, M.; Knox, J. E.; Cross, J. B.; Bakken, V.; Adamo, C.; Jaramillo, J.; Gomperts, R.; Stratmann, R. E.; Yazyev, O.; Austin, A. J.; Cammi, R.; Pomelli, C.; Ochterski, J. W.; Martin, R. L.; Morokuma, K.; Zakrzewski, V. G.; Voth, G. A.; Salvador, P.; Dannenberg, J. J.; Dapprich, S.; Parandekar, P. V.; Mayhall, N. J.; Daniels, A. D.; Farkas, O.; Foresman, J. B.; Ortiz, J. V.; Cioslowski, J.; Fo, D. J.; Gaussian09, Revision D.01; Gaussian, Inc.; Wallingford CT; 2009.

[80] Becke, A. D. A new mixing of hartree−fock and local density−functional theories *J. Chem. Phys.* **1993**, *98*, 1372–1377.

[81] Godbout, N.; Salahub, D. R.; Andzelm, J.; Wimmer, E. Optimization of Gaussian-type basis sets for local spin density functional calculations. Part I. Boron through neon, optimization technique and validation *Can. J. Chem.* **1992**, *70*, 560–571.

[82] Bühl, M.; Kabrede, H. Geometries of Transition-Metal Complexes from Density-Functional Theory *J. Chem. Theory Comput.* **2006**, *2*, 1282–1290.

[83] Determan, J. J.; Poole, K.; Scalmani, G.; Frisch, M. J.; Janesko, B. G.; Wilson, A. K. Comparative Study of Nonhybrid Density Functional Approximations for the Prediction of 3d Transition Metal Thermochemistry *J. Chem. Theory Comput.* **2017**, *13*, 4907–4913.

[84] Moltved, K. A.; Kepp, K. P. Chemical Bond Energies of 3d Transition Metals Studied by Density Functional Theory *J. Chem. Theory Comput.* **2018**, *14*, 3479–3492.

[85] Vega, L.; Ruvireta, J.; Viñes, F.; Illas, F. Jacob's Ladder as Sketched by Escher: Assessing the Performance of Broadly Used Density Functionals on Transition Metal Surface Properties *J. Chem. Theory Comp.* **2018**, *14*, 395–403.

[86] Fantacci, S.; De Angelis, F. A computational approach to the electronic and optical properties of Ru(II) and Ir(III) polypyridyl complexes: Applications to DSC, OLED and NLO *Coord. Chem. Rev.* **2011**, *255*, 2704–2726.

[87] Jorgensen, W. L.; Maxwell, D. S.; Tirado-rives, J. Development and Testing of the OPLS All-Atom Force Field on Conformational Energetics and Properties of Organic Liquids *J. Am. Chem. Soc.* **1996**, *7863*, 11225–11236.

[88] Damm, W.; Frontera, A.; Tirado-Rives, J.; Jorgensen, W. L. OPLS all-atom force field for carbohydrates *J. Comp. Chem.* **1997**, *18*, 1955–1970.

[89] Marenich, A. V.; Jerome, S. V.; Cramer, C. J.; Truhlar, D. G. Charge Model 5: An Extension of Hirshfeld Population Analysis for the Accurate Description of Molecular

Interactions in Gaseous and Condensed Phases *J. Chem. Theory Comput.* **2012**, *8*, 527–541.

[90] Cossi, M.; Barone, V.; Cammi, R.; Tomasi, J. Ab initio study of solvated molecules: a new implementation of the polarizable continuum model *Chem. Phys. Lett.* **1996**, *255*, 327 – 335.

[91] Pronk, S.; Páll, S.; Schulz, R.; Larsson, P.; Bjelkmar, P.; Apostolov, R.; Shirts, M. R.; Smith, J. C.; Kasson, P. M.; van der Spoel, D.; Hess, B.; Lindahl, E. GROMACS 4.5: a High-Throughput and Highly Parallel Open Source Molecular Simulation Toolkit *Bioinformatics* **2013**, *29*, 845–854.

[92] Abraham, M. J.; Murtola, T.; Schulz, R.; Pll, S.; Smith, J. C.; Hess, B.; Lindahl, E. GROMACS: High performance molecular simulations through multi-level parallelism from laptops to supercomputers *SoftwareX* **2015**, *1-2*, 19 – 25.

[93] Berendsen, H. J. C.; Postma, J. P. M.; van Gunsteren, W. F.; DiNola, A.; Haak, J. R. Molecular dynamics with coupling to an external bath *J. Chem. Phys.* **1984**, *81*, 3684–3690.

[94] Bussi, G.; Donadio, D.; Parrinello, M. Canonical sampling through velocity rescaling *J. Chem. Phys.* **2007**, *126*, 014101.

[95] Parrinello, M.; Rahman, A. Polymorphic transitions in single crystals: A new molecular dynamics method *J. Appl. Phys.* **1981**, *52*, 7182–7190.

[96] Maroncelli, M.; Fleming, G. R. Computer simulation of the dynamics of aqueous solvation *J. Chem. Phys.* **1988**, *89*, 5044–5069.

[97] Carter, E. A.; Hynes, J. T. Solvation dynamics for an ion pair in a polar solvent: Time-dependent fluorescence and photochemical charge transfer *J. Chem. Phys.* **1991**, *94*, 5961–5979.

[98] Callen, H. B.; Welton, T. A. Irreversibility and Generalized Noise *Phys. Rev.* **1951**, *83*, 34–40.

[99] Pastore, M.; De Angelis, F.; Angeli, C. Optical absorption spectrum of the N3 solar cell sensitizer by second-order multireference perturbation theory *Theor. Chem. Accounts* **2016**, *135*, 108.

[100] Pastore, M.; De Angelis, F. First-Principles Modeling of a Dye-Sensitized TiO2/IrO2 Photoanode for Water Oxidation *jacs* **2015**, *137*, 5798–5809.

[101] Plasser, F.; Wormit, M.; Dreuw, A. New tools for the systematic analysis and visualization of electronic excitations. I. Formalism *J. Chem. Phys.* **2014**, *141*, 024106.

[102] Plasser, F.; Bäppler, S. A.; Wormit, M.; Dreuw, A. New tools for the systematic analysis and visualization of electronic excitations. II. Applications *J. Chem. Phys.* **2014**, *141*, 024107.

[103] Ando, K.; Kato, S. Dielectric relaxation dynamics of water and methanol solutions associated with the ionization of N, N-dimethylaniline: Theoretical analyses *J. Chem. Phys.* **1991**, *95*, 5966–5982.

[104] Fonseca, T.; Ladanyi, B. M. Breakdown of linear response for solvation dynamics in methanol *J. Phys. Chem.* **1991**, *95*, 2116–2119.

[105] Kumar, P.; Maroncelli, M. Polar solvation dynamics of polyatomic solutes: Simulation studies in acetonitrile and methanol *J. Chem. Phys.* **1995**, *103*, 3038–3060.

[106] Heid, E.; Moser, W.; Schröder, C. On the validity of linear response approximations regarding the solvation dynamics of polyatomic solutes *Phys Chem Chem Phys* **2017**, *19*, 10940–10950.

[107] Chapman, C.; Fee, R.; Maroncelli, M. Measurements of the solute dependence of solvation dynamics in 1-propanol: the role of specific hydrogen-bonding interactions *J. Phys. Chem.* **1995**, *99*, 4811–4819.

[108] Baumann, R.; Ferrante, C.; Kneuper, E.; Deeg, F.-W.; Bräuchle, C. Influence of confinement on the solvation and rotational dynamics of Coumarin 153 in ethanol *J. Phys. Chem. A* **2003**, *107*, 2422–2430.

[109] Heid, E.; Schrder, C. Effect of a Tertiary Butyl Group on Polar Solvation Dynamics in Aqueous Solution: A Computational Approach *J. Phys. Chem. B* **2017**, *121*, 9639–9646.

[110] Gerecke, M.; Richter, C.; Quick, M.; Ioffe, I. N.; Mahrwald, R.; Kovalenko, S. A.; Ernsting, N. P. Effect of a tertiary butyl group on polar solvation dynamics in aqueous solution: Femtosecond fluorescence spectroscopy *J. Phys. Chem. B* **2017**, *121*, 9631–9638.

[111] Kumpulainen, T.; Rosspeintner, A.; Vauthey, E. Probe dependence on polar solvation dynamics from fs broadband fluorescence *Phys. Chem. Chem. Phys.* **2017**, *19*, 8815–8825.

[112] Saiz, L.; Guardia, E.; Padró, J.-À. Dielectric properties of liquid ethanol. A computer simulation study *J. Chem. Phys.* **2000**, *113*, 2814–2822.

[113] Horng, M.; Gardecki, J.; Papazyan, A.; Maroncelli, M. Subpicosecond measurements of polar solvation dynamics: coumarin 153 revisited *J. Phys. Chem.* **1995**, *99*, 17311–17337.

[114] Martins, L. R.; Tamashiro, A.; Laria, D.; Skaf, M. S. Solvation dynamics of coumarin 153 in dimethylsulfoxide–water mixtures: Molecular dynamics simulations *J. Chem. Phys.* **2003**, *118*, 5955–5963.

[115] Vechi, S. M.; Skaf, M. S. Molecular-dynamics simulations of dimethylsulfoxide-methanol mixtures *J. Chem. Phys.* **2005**, *123*, 154507.

[116] Ronca, E.; Angeli, C.; Belpassi, L.; De Angelis, F.; Tarantelli, F.; Pastore, M. Density Relaxation in Time-Dependent Density Functional Theory: Combining Relaxed Density Natural Orbitals and Multireference Perturbation Theories for an Improved Description of Excited States *J. Chem. Theory Comput.* **2014**, *10*, 4014–4024.

[117] Pastore, M.; Assfeld, X.; Mosconi, E.; Monari, A.; Etienne, T. Unveiling the nature of post-linear response Z-vector method for time-dependent density functional theory *J. Chem. Phys.* **2017**, *147*, 024108.

[118] Mayer, U.; Gutmann, V.; Gerger, W. The acceptor number: A quantitative empirical parameter for the electrophilic properties of solvents *Monatshefte für Chemie / Chemical Monthly* **1975**, *106*, 1235–1257.